

# Flat Bands, Topology, and Superconductivity of “Magic” Honeycomb Network in TaS<sub>2</sub>

Jongjun M. Lee,<sup>1</sup> Chenhua Geng,<sup>2</sup> Jae Whan Park,<sup>3</sup> Masaki Oshikawa,<sup>2</sup>

Sung-Sik Lee,<sup>4,5</sup> Han Woong Yeom,<sup>3,1</sup> and Gil Young Cho<sup>1,\*</sup>

<sup>1</sup>*Department of Physics, Pohang University of Science and Technology (POSTECH), Pohang 37673, Republic of Korea*

<sup>2</sup>*Institute for Solid State Physics, The University of Tokyo, Kashiwa, Chiba 277-8581, Japan*

<sup>3</sup>*Center for Artificial Low Dimensional Electronic Systems,*

*Institute for Basic Science (IBS), Pohang 37673, Korea*

<sup>4</sup>*Department of Physics & Astronomy, McMaster University,  
1280 Main St. W., Hamilton ON L8S 4M1, Canada*

<sup>5</sup>*Perimeter Institute for Theoretical Physics, 31 Caroline ST. N., Waterloo ON N2L 2Y5, Canada*

(Dated: May 17, 2022)

We uncover a rich phenomenology of the self-organized honeycomb network superstructure of one-dimensional metals in a nearly-commensurate charge-density wave 1T-TaS<sub>2</sub>, which may play a significant role in understanding global topology of phase diagrams and superconductivity. The key observation is that the emergent honeycomb network magically supports a cascade of flat bands, whose unusual stability we thoroughly investigate. Furthermore, by combining the weak-coupling mean-field and strong-coupling approaches, we argue that the superconductivity will be strongly enhanced in the network. This provides a natural cooperative mechanism of the charge order and superconductivity, which coexist side-by-side in the 1T-TaS<sub>2</sub>. Not only the superconductivity, we show that abundant topological band structures including several symmetry-protected band crossings and corner states, which are closely related to that of the higher-order topology, appear. The results reported here can be generically applicable to various other systems with similar network superstructures.

**1. Introduction:** Topology of electron wavefunctions and strong correlations are the two main resources for modern condensed matter physics to develop and grow.<sup>1–4</sup> The strong electronic correlation is the hidden root of the central enigma in the field, namely the macroscopic coexistence of competing orders. In such a material, spin/charge orders and superconductivity are coherently intertwined<sup>4</sup> at the microscopic scale to form a self-organized superstructure, which is against the conventional wisdom. On the other hand, the discovery<sup>5,6</sup> of the non-trivial topology in electronic states has drastically changed our view on band insulators and left huge impacts on various fields of physics. The two fields have dramatically evolved when a new theoretical/experimental system, which can show the desired topology or correlation phenomena, has been discovered. In this Letter, we theoretically show that the honeycomb network inside the nearly-commensurate charge-density wave state of 1T-TaS<sub>2</sub> is an ideal system to explore both the physics of the diverse topology and understand the coexistence of the charge order and superconductivity

We first uncover an entirely new cooperative mechanism for a charge order and superconductivity in 1T-TaS<sub>2</sub>. Experimentally, it is found to have a rich phase diagram of charge-density wave (CDW) orders<sup>7</sup> and superconductivity (SC),<sup>8–10</sup> which are accessible by tuning temperature, pressure, and doping. Depending on the degree of the charge ordering, there are three distinct regimes: commensurate CDW (C-CDW), nearly-commensurate CDW (NC-CDW), and incommensurate CDW (IC-CDW). The C-CDW phase has a long-ranged charge ordering and appears at the lowest temperature with the ambient pressure. This state is the correlation-

driven Mott insulator,<sup>11</sup> which has been suspected to be the long-sought spin liquid.<sup>12,13</sup> When the C-CDW ordering is slightly suppressed by pressure or doping, then the domain walls appear inbetween the locally charge-ordered domains, i.e., it enters into the NC-CDW state. If the pressure or doping increase further, the SC emerges from this NC-CDW state and they exist side-by-side coherently. This suggests that the NC-CDW<sup>8–10,14,15</sup> is somehow essential for realizing SC in 1T-TaS<sub>2</sub> though how this actually happens has not been clarified.

We will point out that this NC-CDW state and its associated honeycomb network of metallic domain walls<sup>16–18</sup> host a series of robust flat bands, which can greatly help for the SC to emerge. A recent STM study<sup>17</sup> combined with *ab-initio* DFT calculation provided an unprecedented detail of the electronic structure of the network, where the metallic nature of the domain walls and trijunctions in the network is clearly exposed. Motivated by the experiments,<sup>16–18</sup> we consider the emergent electronic states out of this network superstructure, which has been missing so far, and thoroughly examine the stability of the flat bands. Having established the robustness of the flat bands, we consider the correlation-driven many-body phenomena. The effect of the correlation is particularly drastic when the Fermi level is near the flat bands. In this case, we show that the network can strongly enhance the superconducting  $T_c$ . Hence we clarify the long-sought cooperative mechanism between the NC-CDW state and the emerging SC in 1T-TaS<sub>2</sub>. On top of this, we show that the honeycomb network is an outstanding system to realize a long list of topological band structures including two-component Dirac/quadratic band touching,<sup>19</sup> three-component spin-1 Dirac fermion,<sup>20</sup> Chern insulator and

zero-dimensional corner state<sup>21–24</sup> which is closely related to that of higher-order topology.

Our theory of the honeycomb network is not restricted to 1T-TaS<sub>2</sub> but is relevant for other materials accompanying a similar network, e.g. TiSe<sub>2</sub>,<sup>14,15</sup> <sup>3</sup>He and <sup>4</sup>He mixtures adsorbed to graphite,<sup>25–28</sup> a few other chemical compounds,<sup>29–32</sup> and artificially-built network.<sup>33</sup> Below we will explore the physics of this honeycomb network and expose its rich phenomenology.

**2. Model and Flat Bands:** We first present a simple tight-binding model which exposes the essential physics. It consists of the modes inside the CDW gap, which are entirely from the domain wall regions. See Fig 1 (A).

$$H_0 = -t_0 \sum_{\langle \mathbf{r}, \mathbf{r}' \rangle} c_{\mathbf{r}, \sigma}^\dagger c_{\mathbf{r}', \sigma} - t_J \sum_{\{\mathbf{r}, \mathbf{r}'\} \in J} c_{\mathbf{r}, \sigma}^\dagger c_{\mathbf{r}', \sigma} + h.c., \quad (1)$$

where the second sum over  $\{\mathbf{r}, \mathbf{r}'\} \in J$  runs over the sites around the junctions  $J$  and  $t_J \leq t_0$ . Here  $\sigma$  represents the spin and the sum over it is assumed. Here we have assumed the spin rotational symmetry for simplicity. The model also has time-reversal symmetry  $\mathcal{T}$ , reflection  $R_x$ , and six-fold rotation  $C_6$ , which are the symmetries observed in the STM experiment.<sup>17</sup> Diagonalizing Eq.(1), we find a cascade of flat bands, Dirac and quadratic band crossings. See Fig 1 (B). On top of this, a three-component spin-1 Dirac fermion<sup>20</sup> can appear when  $t_J/t_0 \rightarrow 0$ . The number of the flat bands and topological band crossings is proportional to the number of the sites between the junctions. In 1T-TaS<sub>2</sub>,<sup>17</sup> we expect that the energy difference between the neighboring flat bands is roughly 30 meV and there are *at least* 4-5 flat bands (or more) inside the Mott gap. The topological band crossings are protected by crystalline and  $\mathcal{T}$ -symmetries. On the other hand, the flat dispersion cannot be generally protected because it requires infinitely many parameters to be tuned. Hence, they are generically fragile, e.g., against the second neighbor hoppings.<sup>34</sup> Despite of the fragile nature, flat bands are an ideal stage to realize correlation-dominated physics, such as ferromagnetism, and thus have been studied vigorously.<sup>35</sup> A well known general mechanism which gives rise to flat bands is an imbalance between sublattice sites in bipartite lattices. This was also applied<sup>36</sup> to hyperhoneycomb systems which have some similarities with the systems we study in this paper. However, such flat bands can be generically removed by inclusion of short-ranged further neighbor hoppings, which exists in real materials.

Remarkably, our flat bands from the network defy this standard phenomenology and are stable against  $D_6$ -symmetric local perturbations. For example, addition of the third neighbor hoppings  $t_3$  (or even the fourth neighbor hoppings) near the nodes does not disperse the flat bands. Note that  $t_J$  in Eq.(1) is already the second neighbor hoppings. We can even include the insulating electronic states from the domain area (described by  $H_{dom}$ ). See Fig.1 (A). The full Hamiltonian is now

$$H = H_0 + H_{dom} + H_{coup} \text{ with}$$

$$H_{coup} = -t_d \sum_{\langle \mathbf{r}, \mathbf{r}' \rangle} c_{\mathbf{r}, \sigma}^\dagger d_{\mathbf{r}', \sigma} + h.c.,$$

where  $c_{\mathbf{r}, \sigma}$  ( $d_{\mathbf{r}, \sigma}$ ) electrons belong to the network (to the domains). Here  $H_{dom}$  is described by the band insulator which has the two energy-split states per site and the different sites are connected by the small hopping  $t_D$  [Fig. 1 (c)]. From the perturbative reasoning, we expect that this model includes all the possible symmetric local perturbations. Notably, the flat bands and overall band shapes remain almost intact inside the insulating gap [Fig.1 (C)]. This result implies that in the NC-CDW 1T-TaS<sub>2</sub>, even if the bulk bands from the domain region rise up, flat bands inside the gap are almost intact. Finally, we checked that the flat bands survive<sup>34</sup> against the Rashba spin-orbit coupling. Such stability is unique to the honeycomb network and is absent for other network.<sup>34</sup> The above finding is consistent with our previous study.<sup>17</sup> There, we have considered a single-particle scattering problem of the same network where an electron propagates ballistically along 1d wires and scatters at the junctions. This description reflects faithfully the essential features of the band structure of Eq.(1), i.e., the repeated appearance of the flat bands and topological band crossings. Within this description, independent of the specific values of the parameters, we always find the flat bands (the summary is in SI.<sup>34</sup>).

This unusual stability of the flat bands requests some explanation. For this, we look carefully into the structure of the wavefunctions inside the flat bands. We find that those wavefunctions vanish at the junctions.<sup>34</sup> This means that when the low-energy degrees of freedom are entirely from the network and only the nearest neighbor hoppings are included, i.e.,  $t_J = 0$  in Eq.(1), the wavefunction is a standing wave  $\psi(l)$ , e.g.,  $\psi(l) \propto \sin(\frac{\pi l}{L})$  [Fig 2 (A)]. From such standing waves, we can construct a set of localized states<sup>37</sup> which consist of the flat bands: we consider a linear combination around the honeycomb plaquette with a sign oscillation, i.e.,  $\Psi \sim \sum_a (-1)^a \psi(l)$  for  $a \in \{1, 2, \dots, 6\}$  labeling the six links around the plaquette. See the pictorial representation in Fig. 2 (A). It is straightforward to see that this state cannot disperse into the neighboring plaquettes because of the destructive interference. See Fig 2 (A) and its caption. Such destructive interference persists as far as the hopping distance is shorter than the length of the wire. We can also understand that the cascade of the flat bands *must* appear because there are many standing wave solutions per wire. This illustrates the importance of the symmetry and the locality on the stability of the flat bands.

From the above, we expect the flat bands to be removed either by long-ranged direct hopping processes across the CDW domains or by breaking symmetries. Indeed, we can show that the flat bands are lifted when the symmetries are broken [Fig 2 (C) and SI<sup>34</sup>], and/or when such long-ranged hoppings [e.g.,  $t_f$  term in Fig 2 (A)] are included [Fig 2 (B)]. This means that, for the

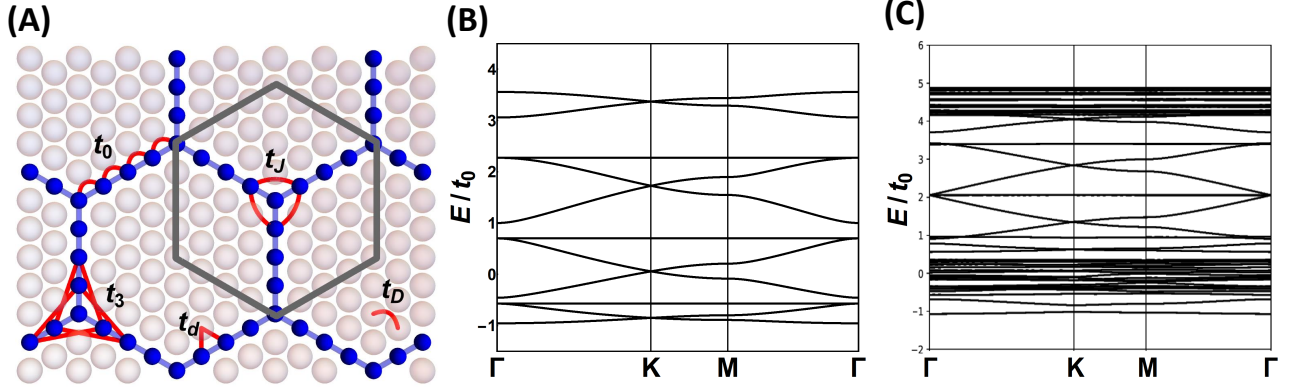


FIG. 1. (Color online) (A) Network of one-dimensional metals inside CDW domains. In Eq.(1), only the sites along the straight blue lines are included. The grey circles represent the region of insulators. The black line represents the unit cell of this superstructure. Here  $t_3$  is the 3rd nearest neighbor hoppings. (B) Typical band structure of the tight-binding models. Note that there is a repeated structure. The lowest three bands, a single flat band and two dispersive bands with Dirac and quadratic band touchings, are roughly repeated (with varying band width). When the bigger number of the bridge sites is considered, the same structure appears more. (C) Band structure when the coupling to the domain regions are included.

NC-CDW state of 1T-TaS<sub>2</sub>, we need a sizable hopping between the two sites apart by  $\sim O(80)\text{\AA}$ <sup>17</sup> to remove the flat bands, which is not realistic. This explains why the dispersion of the “flat bands” are very small but still finite when the domain sites are included (the “dispersion” is induced by the exponentially suppressed but non-zero hoppings through insulating domain sites.). We also note that when the time-reversal symmetry is broken, the band touchings are gapped out and it results in dispersive Chern bands [Fig 2 (C)]. Here, the resulting band width can be still small and thus we find a long-desired relatively-flat Chern band, which is a natural platform for fractional Chern physics.<sup>38</sup> Similarly, we can straightforwardly generalize this to the quantum spin Hall bands.

We comment on the effect<sup>39–42</sup> of the interlayer coupling in 1T-TaS<sub>2</sub>. The interlayer interaction has been suggested to be important in metallization and SC in 1T-TaS<sub>2</sub>. However, we remark that there are plenty of experimental data and theory<sup>13,17</sup> suggesting that the main physics is essentially two-dimensional. For example, the resistivity along  $c$ -axis is much larger, e.g., by 500 times,<sup>43</sup> than the intralayer resistivity<sup>43,44</sup> and anisotropic two-dimensional charge transfer is observed for the NC-CDW state.<sup>45</sup> Further, the SC  $T_c$  is almost insensitive to the pressure<sup>8</sup> and not much affected under the dimensional reduction.<sup>9</sup> Basing on these, we focus on the two-dimensional physics here.

**3. Superconducting States:** Having established the stability of the flat bands, we now discuss the many-body physics when the Fermi level is near one of the flat bands. In general, such system is unstable toward various particle-hole (e.g., ferromagnetism<sup>46</sup>) and particle-particle channels. However, guided by experiments, we mainly focus on SC in this paper.

First, we perform the simplest BCS mean-field theory

with the phenomenological interaction

$$H_{int} = U \sum_{\mathbf{r}} n_{\mathbf{r}}^2 + V \sum_{\langle \mathbf{r}, \mathbf{r}' \rangle} n_{\mathbf{r}} n_{\mathbf{r}'}. \quad (2)$$

Projecting to the BCS channel, we obtain:<sup>34</sup>

$$H_{int} \rightarrow H_{BCS} = \sum_{l \in 2\mathbb{Z}} g_l \sum_{\mathbf{p}, \mathbf{k}} \hat{\Delta}_{l;\mathbf{p}}^\dagger \cdot \hat{\Delta}_{l;\mathbf{k}}, \quad (3)$$

where  $g_l$  is the interaction strength along the pairing channel of the angular momentum  $l$ , which we compute numerically.  $\hat{\Delta}_{l;\mathbf{p}}$  is the corresponding pairing order parameter. Note that, within the mean-field decomposition of Eq.(2), only the spin-singlet sector appears. Below we consider only the  $s$ -wave and  $(d + id)$ -wave pairing channels, i.e.,  $g_0$  and  $g_2 = g_{-2}$  of Eq.(3). We find that typically  $\{g_0, g_2\}$  are positive when  $U$  is large and positive. However, as the negative  $V$  is added,  $g_0$  and  $g_2$  decrease toward negative and signal the instability toward the superconducting states. As the negative  $V$  increases, generically  $g_2$  first becomes negative and thus it opens up a window for the  $(d \pm id)$ -channel pairing. If  $U$  and  $V$  are both negative, then typically  $g_0$  is more negative than  $g_2$  and the  $s$ -wave pairing is favored. The phase diagram including the ferromagnetism (which appears when the interactions are dominantly repulsive) is in SI.<sup>34</sup>

The magic of the flat bands appears when the gap equation is solved.

$$\frac{1}{g_l} \sim \int_{\text{BZ}} \frac{d^2 k |F_l(\mathbf{k})|^2}{\sqrt{(\epsilon_k - \mu)^2 + |F_l(\mathbf{k})\Delta_l|^2}} \sim \frac{1}{|\Delta_l|},$$

where  $F_l(\mathbf{k})$  is the form factor for each pairing channels,<sup>34</sup> e.g.,  $F_2(\mathbf{k}) \rightarrow (k_x + ik_y)^2$  for  $|\mathbf{k}| \ll 1$ , and  $\epsilon_k = \mu$ . Hence, we find that the SC gap is linearly enhanced, i.e.,  $|\Delta_l| \sim |g_l|$  (if  $g_l < 0$ ), instead of the standard exponential

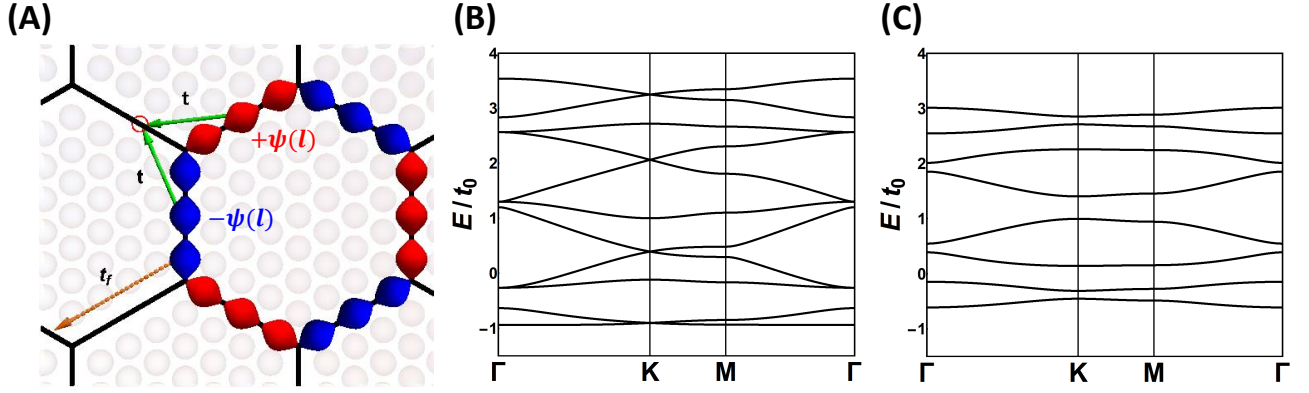


FIG. 2. (Color online) (A) Localized States in Flat Bands. Each state in flat bands consists of standing waves living in links. The standing waves receive  $\pm 1$  around the plaquette  $\Psi_a(l) \sim (-1)^a \psi(l)$ . Here the red colored waves are with  $(-1)$  sign and the blue colored waves are with  $(+1)$  sign. When the state attempts to hop to the next plaquette, there are two contributions: one from the blue one  $t \times (-\psi(l))$  and the other from the red one  $t \times (+\psi(l))$ . When summed up, they exactly cancel. (B) Typical band structure when the hopping across the domain is added. For this process, there is no destructive interference and so the flat bands become dispersive. (C) Band structure with the broken  $\mathcal{T}$ -symmetry. In this case, all the band touchings are removed and the flat bands become dispersive. Furthermore, all the bands carry the non-zero Chern numbers.

suppression  $\sim \exp(-1/|g_l|\nu_l)$ . Because there is no other scale, the mean-field energy of the SC is linear in  $g_l$  and so is the  $T_c$ .<sup>34</sup> Hence, the honeycomb network strongly enhances the SC  $T_c$ .

In the  $s$ -wave SC, the BdG fermion is fully gapped as usual. On the other hand, the  $(d \pm id)$ -wave SC is not fully gapped and exhibits the doubled quadratic band touching.<sup>34</sup> Since this state is gapless, it does not support any topologically-protected edge mode. Because the quadratic band touching is marginally unstable<sup>19</sup> against the short-ranged repulsive interactions toward the chiral or nematic states, there will be a successive transition at the temperatures below the SC  $T_c$ .

On the other hand, it also instructive to consider the strong-coupling limit of the network,<sup>47</sup> where the interaction is bigger than the hopping integrals. For this, we start from the decoupled *strongly-correlated* wires, each of which may be described by a Tomonaga-Luttinger liquid (TLL)

$$H = \sum_{a,\sigma=c/s} \int dl \frac{v_\sigma}{2} \left[ \frac{1}{K_\sigma} (\partial_l \theta_{a,\sigma})^2 + K_\sigma (\partial_l \phi_{a,\sigma})^2 \right],$$

where the Luttinger parameters  $\{K_c, K_s\}$  capture the correlation non-perturbatively.<sup>2</sup> This is the correlated version of the scattering problem in our previous work,<sup>17</sup> which faithfully represented the band structures.

The two-dimensional SC can be preempted by the spin gap<sup>2,48</sup> in each wire. Once the spin gap forms, the low-energy physics of each wire is described by a single-component TLL of  $\theta_{a,c}$  describing the fluctuating SC pairs.<sup>2</sup> Since the SC pair is bosonic, the junction of three TLLs at each vertex of the honeycomb network corresponds to the bosonic Y-junction,<sup>49</sup> rather than the fermionic one<sup>50,51</sup> where the fermion statistics plays an important role. When each wire has sufficient attraction, i.e.,  $K_c \leq 1$ ,<sup>2</sup> then the interwire coupling between

the SC fluctuations, namely the Josephson coupling  $J$ , becomes relevant.<sup>2</sup> This will lock the spatial pattern of the phases of the SC fluctuations between different wires. Only interested in the pattern of the phases, we simply note that the problem is symmetrically equivalent to the XY model on the *Kagome* lattice, while leaving the full quasi-1d interchain mean-field treatment<sup>48</sup> to the future study

$$H_{eff} = J \sum_{\langle i,j \rangle} \left[ e^{\sqrt{2}\pi i(\theta_{i,c} - \theta_{j,c})} + h.c. \right] \quad (4)$$

Depending on the sign of  $J$ , either the two-dimensional  $s$ -wave or  $(d \pm id)$ -wave SCs can emerge from these fluctuations. When  $J > 0$ , then the so-called  $\sqrt{3} \times \sqrt{3}$  order appears,<sup>52</sup> which translates as the  $(d \pm id)$ -SC. If  $J < 0$ , the conventional  $s$ -wave SC emerges. When the repulsive- $U$  dominates the junction region and the region becomes Mott insulating,<sup>53</sup>  $J > 0$  can appear. From this strong-coupling limit, we can learn how the  $2k_F$ -density wave of 1d wires competing with SC is suppressed. For generic filling of the flat bands, the momentum  $k_F$  will not be commensurate with the wire length  $L$ , i.e.,  $\phi_L = k_F L$  is not a rational number. This will frustrate the phases of the density waves, and thus their true two-dimensional order is strongly suppressed to develop. This gives a natural favor on the SC over insulators.

When the filling per wire is commensurate, then the network can develop a charge density wave order and become an insulator. This can lead to the emergent corner states at the tri-junctions and corners of the sample boundary, which are akin to those of higher-order topological insulators.<sup>21–23</sup> Motivated by references<sup>54,55</sup> where the nature of the insulating domain walls of C-CDW 1T-TaS<sub>2</sub> were discussed, we consider the half-filled wires which can develop a period-2 charge density modulation. When the tri-junction frustrates the charge order



and traps solitons, we can show that there is an associated crystal symmetry-protected bound state at the junction (In SI,<sup>34</sup> we provide a few concrete realizations.). By passing, we note that gapped domain wall junctions in the C-CDW state 1T-TaS<sub>2</sub> are found experimentally.<sup>54</sup>

**4. Conclusions:** In this Letter, we have considered the electronic structure of a conducting honeycomb network observed in the NC-CDW state 1T-TaS<sub>2</sub>. We have constructed a lattice model and uncovered the emergence of the cascade of the flat bands. Combining the scattering theory,<sup>17</sup> tight-binding calculation and also the analytical reasoning, we have established and explained the emergence of many flat bands stable against various local perturbations. Compared to the previous studies, the discovery and analysis of many stable flat bands are unprecedented. Not only the flat bands, we also demonstrated that the honeycomb network is an ideal place to find diverse topological band structures: the regular Dirac and spin-1 Dirac fermions, quadratic band touchings, Chern insulators, topological band insulators, and also zero-dimensional corner states.

When the chemical potential is tuned near one of the flat bands, the many-body effects are enhanced. Motivated by 1T-TaS<sub>2</sub>, we have concentrated on the SC states and have discovered the anomalous enhancement of SC  $T_c$ . In both the weak-coupling mean-field and strong-coupling Luttinger liquid limits, we found that the *nodal* ( $d \pm id$ )-SC can emerge when the repulsive- $U$  plays significant role, e.g., suppressing  $s$ -wave SC to emerge. When the on-site  $U$  is attractive, the system enters into the  $s$ -wave state. Given that the domain wall states of 1T-TaS<sub>2</sub> presumably experience small correlation effect and that the junction regions are quite metallic from the STM data,<sup>17</sup> our result suggests that the SC state of 1T-TaS<sub>2</sub> is likely a regular  $s$ -wave SC (with some  $p$ -wave component due to the spin-orbit coupling). We remark that the strong enhancement of the SC by the NC-CDW network discovered in this paper provides a new example of the so-called “intertwinement” of the orders. This is clearly beyond the previous bosonic analysis, e.g., Landau-Ginzburg theory<sup>15</sup> or non-linear  $\sigma$  models, which are blind to these emergent electronics from the network superstructure. Also our work here clarifies

the precise role of the domain wall network of the CDW 1T-TaS<sub>2</sub> in realizing SC and explains how the two seemingly-competing orders coexist and self-organize.

The signature of the network and its role in SC can be detected in various experiments. First, inside the normal state, photo-emission experiment can in principle access the emergent band spectrum. Within the currently-available experimental data,<sup>56–58</sup> we find that it is unclear either to confirm or to rule out the existence of the cascade of the flat bands in 1T-TaS<sub>2</sub>. At least one nearly flat band is observed right below the chemical potential. This calls for further investigation. Second, magneto-transport and oscillations in resistivity of the normal state and SC state can provide the information about the primary conducting and SC channels. They have been applied in the small twist-angle bilayer graphene<sup>59,60</sup> and textured superconducting states of TiSe<sub>2</sub><sup>14,15</sup> to identify the network geometry. Also the flat bands show a few characteristic behaviors in thermodynamic quantities, which we summarize in SI.<sup>34</sup>

## ACKNOWLEDGMENTS

We thank Peter Abbamonte, Ehud Altman, Liang Fu, Hiroshi Fukuyama, Jung-Hoon Han, Tim Hsieh, Eun-Ah Kim, Yong Baek Kim, Jong Hwan Kim, Hae Young Kee, Tae Hwan Kim, Sungbin Lee, Ivar Martin, Masashi Morishita, Adrian Po, Youngwoo Son, Dam T. Son, Ashvin Vishwanath, and Mike Zaletel for helpful discussion. The research of S. L. was supported by NSERC. Research at the Perimeter Institute is supported in part by the Government of Canada through Industry Canada, and by the Province of Ontario through the Ministry of Research and Information. C. G. and M. O. were supported in part by MEXT/JSPS KAKENHI Grant Numbers JP18H03686 and JP17H06462. J.W. P. and H.W.Y are supported by Insitute for Basic Science (IBS-R014-D1). G.Y.C thanks the support by Visiting Fellowship at the Perimeter Institute. Part of this work is done during the winter program “New Approaches to Strongly Correlated Quantum Systems” at Aspen Center for Physics.

---

\* Electronic Address: gilyoungcho@postech.ac.kr

<sup>1</sup> Subir Sachdev, “Quantum phase transitions,” Handbook of Magnetism and Advanced Magnetic Materials (2007).

<sup>2</sup> Eduardo Fradkin, *Field theories of condensed matter physics* (Cambridge University Press, 2013).

<sup>3</sup> Xiao-Gang Wen, *Quantum field theory of many-body systems: from the origin of sound to an origin of light and electrons* (Oxford University Press on Demand, 2004).

<sup>4</sup> Eduardo Fradkin, Steven A. Kivelson, and John M. Tranquada, “Colloquium: Theory of intertwined orders in high temperature superconductors,” *Rev. Mod. Phys.* **87**, 457–482 (2015).

<sup>5</sup> Xiao-Liang Qi and Shou-Cheng Zhang, “Topological insulators and superconductors,” *Rev. Mod. Phys.* **83**, 1057–1110 (2011).

<sup>6</sup> M. Z. Hasan and C. L. Kane, “Colloquium: Topological insulators,” *Rev. Mod. Phys.* **82**, 3045–3067 (2010).

<sup>7</sup> JI A Wilson, FJ Di Salvo, and S Mahajan, “Charge-density waves and superlattices in the metallic layered transition metal dichalcogenides,” *Advances in Physics* **24**, 117–201 (1975).

<sup>8</sup> Balazs Sipo, Anna F Kusmartseva, Ana Akrap, Helmut Berger, Laszlo Forró, and Eduard Tutiš, “From mott state to superconductivity in 1t-tas 2,” *Nature materials* **7**, 960

- (2008).
- <sup>9</sup> Yijun Yu, Fangyuan Yang, Xiu Fang Lu, Ya Jun Yan, Yong-Heum Cho, Liguang Ma, Xiaohai Niu, Sejoong Kim, Young-Woo Son, Donglai Feng, *et al.*, “Gate-tunable phase transitions in thin flakes of 1t-tas<sub>2</sub>,” *Nature nanotechnology* **10**, 270 (2015).
  - <sup>10</sup> Y. Liu, D. F. Shao, L. J. Li, W. J. Lu, X. D. Zhu, P. Tong, R. C. Xiao, L. S. Ling, C. Y. Xi, L. Pi, H. F. Tian, H. X. Yang, J. Q. Li, W. H. Song, X. B. Zhu, and Y. P. Sun, “Nature of charge density waves and superconductivity in 1t-tas<sub>2-x</sub>te<sub>x</sub>,” *Phys. Rev. B* **94**, 045131 (2016).
  - <sup>11</sup> P Fazekas and E Tosatti, “Charge carrier localization in pure and doped 1t-tas<sub>2</sub>,” *Physica B+ C* **99**, 183–187 (1980).
  - <sup>12</sup> KT Law and Patrick A Lee, “1t-tas<sub>2</sub> as a quantum spin liquid,” *Proceedings of the National Academy of Sciences* **114**, 6996–7000 (2017).
  - <sup>13</sup> Wen-Yu He, Xiao Yan Xu, Gang Chen, K. T. Law, and Patrick A. Lee, “Spinon fermi surface in a cluster mott insulator model on a triangular lattice and possible application to 1t-tas<sub>2</sub>,” *Phys. Rev. Lett.* **121**, 046401 (2018).
  - <sup>14</sup> LJ Li, ECT Ofarrell, KP Loh, Goki Eda, B Özyilmaz, and AH Castro Neto, “Controlling many-body states by the electric-field effect in a two-dimensional material,” *Nature* **529**, 185 (2016).
  - <sup>15</sup> Chuan Chen, Lei Su, AH Castro Neto, and Victor M Pereira, “Discommensuration-driven superconductivity in the charge density wave phases of transition-metal dichalcogenides,” *Physical Review B* **99**, 121108 (2019).
  - <sup>16</sup> Albert Spijkerman, Jan L. de Boer, Auke Meetsma, Gerrit A. Wieggers, and Sander van Smaalen, “X-ray crystal-structure refinement of the nearly commensurate phase of 1t-tas<sub>2</sub> in (3+2)-dimensional superspace,” *Phys. Rev. B* **56**, 13757–13767 (1997).
  - <sup>17</sup> Jae Whan Park, Gil Young Cho, Doohee Cho, Jinwon Lee, and Han Woong Yeom, “Emergent honeycomb network of topological excitations in correlated charge density wave,” in preparation.
  - <sup>18</sup> Xian Liang Wu and Charles M Lieber, “Hexagonal domain-like charge density wave phase of tas<sub>2</sub> determined by scanning tunneling microscopy,” *Science* **243**, 1703–1705 (1989).
  - <sup>19</sup> Kai Sun, Hong Yao, Eduardo Fradkin, and Steven A. Kivelson, “Topological insulators and nematic phases from spontaneous symmetry breaking in 2d fermi systems with a quadratic band crossing,” *Phys. Rev. Lett.* **103**, 046811 (2009).
  - <sup>20</sup> Balázs Dóra, Janik Kailasvuori, and Roderich Moessner, “Lattice generalization of the dirac equation to general spin and the role of the flat band,” *Physical Review B* **84**, 195422 (2011).
  - <sup>21</sup> Wladimir A. Benalcazar, B. Andrei Bernevig, and Taylor L. Hughes, “Quantized electric multipole insulators,” *Science* **357**, 61–66 (2017).
  - <sup>22</sup> Frank Schindler, Ashley M. Cook, Maia G. Vergniory, Zhi-jun Wang, Stuart S. P. Parkin, B. Andrei Bernevig, and Titus Neupert, “Higher-order topological insulators,” *Science Advances* **4** (2018), 10.1126/sciadv.aat0346.
  - <sup>23</sup> Frank Schindler, Zhi-jun Wang, Maia G Vergniory, Ashley M Cook, Anil Murani, Shamashis Sengupta, Alik Yu Kasumov, Richard Deblock, Sangjun Jeon, Ilya Drozdov, Hlne Bouchiat, Sophie Gurun, Ali Yazdani, B. Andrei Bernevig, and Titus Neupert, “Higher-order topology in bismuth,” *Nature Physics* **14**, 918 (2018).
  - <sup>24</sup> Byungmin Kang, Ken Shiozaki, and Gil Young Cho, “Many-body invariants for multipoles in higher-order topological insulators,” arXiv preprint arXiv:1812.06999 (2018).
  - <sup>25</sup> Masashi Morishita, “Heat capacity of dilute 3he–4he films on graphite,” *Journal of Low Temperature Physics* **171**, 664–669 (2013).
  - <sup>26</sup> Masashi Morishita, “Heat capacity of dilute <sup>3</sup>he–<sup>4</sup>he monolayer films,” *Journal of Low Temperature Physics* **183**, 245–250 (2016).
  - <sup>27</sup> Masashi Morishita, “1d fermions and dirac fermions in helium film,” (2016), presentation at the 71st Japanese Physical Society Annual Meeting.
  - <sup>28</sup> Masashi Morishita, (2017), private communications.
  - <sup>29</sup> Cyrille Barreteau, Francois Ducastelle, and Talal Mallah, “A birds eye view on the flat and conic band world of the honeycomb and kagome lattices: towards an understanding of 2d metal-organic frameworks electronic structure,” *Journal of Physics: Condensed Matter* **29**, 465302 (2017).
  - <sup>30</sup> Hao Sun, Bin Li, and Jin Zhao, “Half-metallicity in 2d organometallic honeycomb frameworks,” *Journal of Physics: Condensed Matter* **28**, 425301 (2016).
  - <sup>31</sup> Liu Zheng, Liu Feng, and Wu Yong-Shi, “Exotic electronic states in the world of flat bands: From theory to material,” *Chinese Physics B* **23**, 077308 (2014).
  - <sup>32</sup> Mina Maruyama, Nguyen Thanh Cuong, and Susumu Okada, “Coexistence of dirac cones and kagome flat bands in a porous graphene,” *Carbon* **109**, 755–763 (2016).
  - <sup>33</sup> Li-kun Shi, Jing Ma, and Justin CW Song, “Gate-tunable flat bands in van der waals patterned dielectric superlattices,” arXiv preprint arXiv:1904.07877 (2019).
  - <sup>34</sup> See the Supplemental Information for details.
  - <sup>35</sup> Daniel Leykam, Alexei Andreanov, and Sergej Flach, “Artificial flat band systems: from lattice models to experiments,” *Advances in Physics: X* **3**, 1473052 (2018), <https://doi.org/10.1080/23746149.2018.1473052>.
  - <sup>36</sup> Nobuyuki Shima and Hideo Aoki, “Electronic structure of super-honeycomb systems: A peculiar realization of semimetal/semiconductor classes and ferromagnetism,” *Phys. Rev. Lett.* **71**, 4389–4392 (1993).
  - <sup>37</sup> Doron L. Bergman, Congjun Wu, and Leon Balents, “Band touching from real-space topology in frustrated hopping models,” *Phys. Rev. B* **78**, 125104 (2008).
  - <sup>38</sup> Evelyn Tang, Jia-Wei Mei, and Xiao-Gang Wen, “High-temperature fractional quantum hall states,” *Phys. Rev. Lett.* **106**, 236802 (2011).
  - <sup>39</sup> T Ritschel, J Trinckauf, K Koepernik, B Büchner, M v Zimmermann, H Berger, YI Joe, P Abbamonte, and J Geck, “Orbital textures and charge density waves in transition metal dichalcogenides,” *Nature physics* **11**, 328 (2015).
  - <sup>40</sup> T Ritschel, H Berger, and J Geck, “Stacking-driven gap formation in layered 1t-tas<sub>2</sub>,” *Physical Review B* **98**, 195134 (2018).
  - <sup>41</sup> L Le Guyader, T Chase, AH Reid, RK Li, D Svetin, X Shen, T Vecchione, XJ Wang, D Mihailovic, and HA Dürr, “Stacking order dynamics in the quasi-two-dimensional dichalcogenide 1 t-tas<sub>2</sub> probed with mev ultrafast electron diffraction,” *Structural Dynamics* **4**, 044020 (2017).
  - <sup>42</sup> Sung-Hoon Lee, Jung Suk Goh, and Doohee Cho, “Origin of the insulating phase and first-order metal-insulator transition in 1t-tas<sub>2</sub>,” *Phys. Rev. Lett.* **122**, 106404 (2019).

- <sup>43</sup> Paul D Hambourger and FJ Di Salvo, “Electronic conduction process in 1t-tas<sub>2</sub>,” *Physica B+ C* **99**, 173–176 (1980).
- <sup>44</sup> Damjan Svetin, Igor Vaskivskiy, Serguei Brazovskii, and Dragan Mihailovic, “Three-dimensional resistivity and switching between correlated electronic states in 1t-tas<sub>2</sub>,” *Scientific reports* **7**, 46048 (2017).
- <sup>45</sup> Danilo Kühn, Moritz Müller, Florian Sorgenfrei, Erika Giangrisostomi, Raphael M Jay, Ruslan Ovsyannikov, Nils Mörtensson, Daniel Sánchez-Portal, and Alexander Föhlisch, “Directional sub-femtosecond charge transfer dynamics and the dimensionality of 1t-tas<sub>2</sub>,” *Scientific reports* **9**, 488 (2019).
- <sup>46</sup> Hal Tasaki, “Ferromagnetism in the hubbard models with degenerate single-electron ground states,” *Phys. Rev. Lett.* **69**, 1608–1611 (1992).
- <sup>47</sup> Xiao-Chuan Wu, Chao-Ming Jian, and Cenke Xu, “Coupled-wire description of the correlated physics in twisted bilayer graphene,” *Physical Review B* **99**, 161405 (2019).
- <sup>48</sup> Steven A Kivelson, Eduardo Fradkin, and Victor J Emery, “Electronic liquid-crystal phases of a doped mott insulator,” *Nature* **393**, 550 (1998).
- <sup>49</sup> Akiyuki Tokuno, Masaki Oshikawa, and Eugene Demler, “Dynamics of one-dimensional bose liquids: Andreev-like reflection at  $y$  junctions and the absence of the aharonov-bohm effect,” *Phys. Rev. Lett.* **100**, 140402 (2008).
- <sup>50</sup> Claudio Chamon, Masaki Oshikawa, and Ian Affleck, “Junctions of three quantum wires and the dissipative hofstadter model,” *Phys. Rev. Lett.* **91**, 206403 (2003).
- <sup>51</sup> Masaki Oshikawa, Claudio Chamon, and Ian Affleck, “Junctions of three quantum wires,” *Journal of Statistical Mechanics: Theory and Experiment* **2006**, P02008 (2006).
- <sup>52</sup> Jan N. Reimers and A. J. Berlinsky, “Order by disorder in the classical heisenberg kagomé antiferromagnet,” *Phys. Rev. B* **48**, 9539–9554 (1993).
- <sup>53</sup> Erez Berg, Eduardo Fradkin, Steven A Kivelson, and John M Tranquada, “Striped superconductors: how spin, charge and superconducting orders intertwine in the cuprates,” *New Journal of Physics* **11**, 115004 (2009).
- <sup>54</sup> Doohee Cho, Gyeongcheol Gye, Jinwon Lee, Sung-Hoon Lee, Lihai Wang, Sang-Wook Cheong, and Han Woong Yeom, “Correlated electronic states at domain walls of a mott-charge-density-wave insulator 1 t-tas<sub>2</sub>,” *Nature communications* **8**, 392 (2017).
- <sup>55</sup> Jan Skolimowski, Yaroslav Gerasimenko, and Rok Žitko, “Mottness collapse without metallization in the domain wall of the triangular-lattice mott insulator 1t – tas<sub>2</sub>,” *Phys. Rev. Lett.* **122**, 036802 (2019).
- <sup>56</sup> Qing Hu, Cong Yin, Leilei Zhang, Li Lei, Zhengshang Wang, Zhiyu Chen, Jun Tang, and Ran Ang, “Direct observation of melted mott state evidenced from raman scattering in 1t-tas<sub>2</sub> single crystal,” *Chinese Physics B* **27**, 017104 (2018).
- <sup>57</sup> L Perfetti, PA Loukakos, M Lisowski, U Bovensiepen, H Berger, S Biermann, PS Cornaglia, A Georges, and M Wolf, “Time evolution of the electronic structure of 1 t- tas<sub>2</sub> through the insulator-metal transition,” *Physical review letters* **97**, 067402 (2006).
- <sup>58</sup> C Sohrt, A Stange, M Bauer, and K Rossnagel, “How fast can a peierls–mott insulator be melted?” *Faraday discussions* **171**, 243–257 (2014).
- <sup>59</sup> Peter Rickhaus, John Wallbank, Sergey Slizovskiy, Riccardo Pisoni, Hiske Overweg, Yongjin Lee, Marius Eich, Ming-Hao Liu, Kenji Watanabe, Takashi Taniguchi, *et al.*, “Transport through a network of topological channels in twisted bilayer graphene,” *Nano letters* **18**, 6725–6730 (2018).
- <sup>60</sup> Dmitry K Efimkin and Allan H MacDonald, “Helical network model for twisted bilayer graphene,” *Physical Review B* **98**, 035404 (2018).

# Supplemental Information for “Flat Bands, Topology, and Superconductivity of “Magic” Honeycomb Network in TaS<sub>2</sub>”

Jongjun M. Lee and Gil Young Cho\*

*Department of Physics, Pohang University of Science and Technology (POSTECH), Pohang 37673, Republic of Korea*

Chenhua Geng and Masaki Oshikawa

*Institute for Solid State Physics, The University of Tokyo, Kashiwa, Chiba 277-8581, Japan*

Jae Whan Park

*Center for Artificial Low Dimensional Electronic Systems,  
Institute for Basic Science (IBS), Pohang 37673, Korea*

Sung-Sik Lee

*Department of Physics & Astronomy, McMaster University,  
1280 Main St. W., Hamilton ON L8S 4M1, Canada and  
Perimeter Institute for Theoretical Physics, 31 Caroline ST. N., Waterloo ON N2L 2Y5, Canada*

Han Woong Yeom

*Center for Artificial Low Dimensional Electronic Systems,  
Institute for Basic Science (IBS), Pohang 37673, Korea and  
Department of Physics, Pohang University of Science and Technology (POSTECH), Pohang 37673, Republic of Korea*

(Dated: May 17, 2022)

## CONTENTS

A. Details of Scattering Description of Honeycomb Network	2
1. Model	2
2. Spectrum of Network	3
B. Flat Band Wavefunctions	3
1. Presence of Zeros at Tri-junctions	3
2. Proof of Existence of A Single Flat Band	4
C. Flat Bands with Rashba Spin-Orbit Coupling	5
D. No Stable Flat Bands for Triangular and Square Networks	6
E. Effect of Crystal Symmetry Breaking on Flat Bands	6
F. Details of BCS Calculations	7
1. Coupling Constants	7
2. Mean-Field Solution and Energy	9
3. BdG Fermion Spectrum	12
G. Corner States at Tri-Junctions	12
1. Tight-Binding Models	13
H. Thermodynamics of Flat Bands	14
1. Specific Heat	14
2. Spin Susceptibility	14
References	15



## Appendix A: Details of Scattering Description of Honeycomb Network

Here we summarize the theory part of our previous work<sup>1</sup>. Specifically, we will introduce the scattering description of the honeycomb network, which reproduces the key structure of the tight-binding model in the main text.

The STM experiment<sup>1</sup> essentially found that the domains of the nearly-commensurate charge-density wave form a regular honeycomb lattice, and thus the domain walls are the links of this regular honeycomb lattice. Furthermore, the domain walls trap finite local density of states near the Fermi level. We note that the domain walls are generically expected to trap some in-gap modes due to the topological solitonic modes (though these modes may appear away from the Fermi level.). Motivated from these findings, we consider a regular array of one-dimensional metals living on the links of a honeycomb lattice. Similar network models of one-dimensional metals have been studied in the context of quantum Hall plateau transition, known as “Chalker-Coddington model”<sup>2</sup>, and also in the twisted bilayer graphene at a small twisting angle<sup>3</sup>.

### 1. Model

To capture the physics of the network, we introduce the two wavefunctions on the links of the honeycomb network:  $\psi_a$  and  $\psi_{\bar{a}}$ . Here  $\psi_a$  represent the chiral mode propagating from an A-sublattice (of the network) to a B-sublattice (of the network) and  $\psi_{\bar{a}}$  for the mode propagating from a B-sublattice to an A-sublattice. See Fig. 1.

Hence, we can associate  $\psi_a$  to the node at an A-sublattice and  $\psi_{\bar{a}}$  to the node at a B-sublattice, i.e.,  $\psi_a$  is an out-going mode along the link  $a = x, y, z$  from an A-sublattice, and  $\psi_{\bar{a}}$  is an out-going mode along the link  $a = x, y, z$  from a B-sublattice (See Fig. 1).

We further assume that these modes propagate ballistically within each link and scatter only at the nodes of the honeycomb lattice. We further assume that there are six-fold rotation  $C_6$ , mirror  $R_x$ , and  $\mathcal{T}$  symmetries, and the scattering between the modes respects the symmetries. (As in the main text, we assume SU(2) spin rotational symmetry and suppress the spin indices here.)

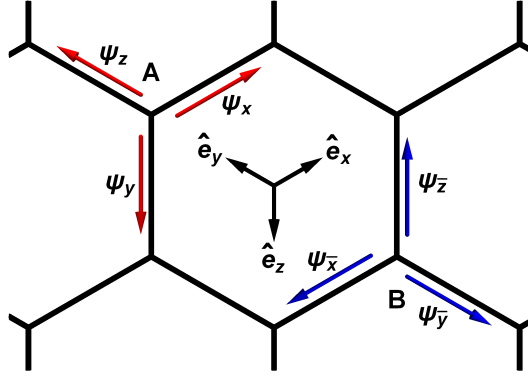


FIG. 1. Pictorial Representation of Network Model.

With all of these in hand, we can write down the scattering problem at an A-sublattice.

$$\begin{bmatrix} \psi_x(\mathbf{R}) \\ \psi_y(\mathbf{R}) \\ \psi_z(\mathbf{R}) \end{bmatrix} = e^{-i\frac{E}{v_F\hbar}L} \cdot \hat{T}_A \cdot \begin{bmatrix} \psi_{\bar{x}}(\mathbf{R} + \hat{e}_x) \\ \psi_{\bar{y}}(\mathbf{R} + \hat{e}_y) \\ \psi_{\bar{z}}(\mathbf{R} + \hat{e}_z) \end{bmatrix} \quad (\text{A1})$$

Here, the left-hand side  $\psi_a(\mathbf{R})$ ,  $a = x, y, z$  represents the out-going modes from the A-sublattice, which is related by a scattering matrix  $\hat{T}_A$  to the in-coming modes  $\psi_{\bar{a}}(\mathbf{R})$ ,  $a = x, y, z$  appearing on the right-hand side (See Fig. 1). The additional phase factor  $\sim \exp(-i\frac{E}{v_F\hbar}L)$  is the phase accumulated by the incoming modes while it propagates coherently from the neighboring B-sublattices to the A-sublattice at  $\mathbf{R}$ . Here  $v_F$  is the Fermi velocity within the one-dimensional metal, which is expected to be similar to that of the bulk electron, and  $L$  is the length of the link. The scattering matrix  $\hat{T}_A$  is fixed by the combination of the crystal symmetries and  $\mathcal{T}$ -symmetry. With the unitarity

of the scattering matrix, we find

$$\hat{T}_A = e^{i\chi_A} \begin{bmatrix} T_A & t_A & t_A \\ t_A & T_A & t_A \\ t_A & t_A & T_A \end{bmatrix}, \quad |T_A| \in \left[\frac{1}{3}, 1\right], \quad t_A = e^{i\phi_A} \sqrt{\frac{1 - |T_A|^2}{2}}, \quad (\text{A2})$$

with  $\phi_A = \cos^{-1}(\frac{|t_A|}{2|T_A|})$ . Similary we have the following scattering problem at the B-sublattice.

$$\begin{bmatrix} \psi_{\bar{x}}(\mathbf{R}) \\ \psi_{\bar{y}}(\mathbf{R}) \\ \psi_{\bar{z}}(\mathbf{R}) \end{bmatrix} = e^{-i\frac{E}{v_F\hbar}L} \cdot \hat{T}_B \cdot \begin{bmatrix} \psi_x(\mathbf{R} - \hat{e}_x) \\ \psi_y(\mathbf{R} - \hat{e}_y) \\ \psi_z(\mathbf{R} - \hat{e}_z) \end{bmatrix}, \quad (\text{A3})$$

where  $\hat{T}_B = \hat{T}_A$  by the crystal symmetries. Now we can perform the Fourier transformation and solve these scattering problems. On performing the Fourier transformation, we find

$$\Psi_{\mathbf{q}} = e^{-i\frac{E_{\mathbf{q}}}{v_F\hbar}L} \hat{T}_{\mathbf{q}} \cdot \Psi_{\mathbf{q}}, \quad \Psi_{\mathbf{q}} = \begin{bmatrix} \psi_x(\mathbf{q}) \\ \psi_y(\mathbf{q}) \\ \psi_z(\mathbf{q}) \\ \psi_{\bar{x}}(\mathbf{q}) \\ \psi_{\bar{y}}(\mathbf{q}) \\ \psi_{\bar{z}}(\mathbf{q}) \end{bmatrix}, \quad \hat{T}_{\mathbf{q}} = \begin{bmatrix} 0 & \hat{T}_A \cdot \hat{V}_{\mathbf{q}} \\ \hat{T}_B \cdot \hat{V}_{\mathbf{q}}^* & 0 \end{bmatrix}, \quad (\text{A4})$$

where  $\hat{V}_{\mathbf{q}} = \text{diag} [\exp(i\mathbf{q} \cdot \hat{e}_x), \exp(i\mathbf{q} \cdot \hat{e}_y), \exp(i\mathbf{q} \cdot \hat{e}_z)]$ . Hence, the energy spectrum can be obtained by diagonalizing  $\hat{T}_{\mathbf{q}}$ , which is unitary. In terms of the eigenvalues  $e^{i\epsilon_j(\mathbf{q})}$ ,  $j = 1, 2, \dots, 6$  of  $\hat{T}_{\mathbf{q}}$ , we have

$$E_{j,\mathbf{q}}^n = 2\pi \frac{v_F\hbar}{L} n + \frac{v_F\hbar}{L} \epsilon_j(\mathbf{q}), \quad j = 1, 2, \dots, 6 \quad (\text{A5})$$

Here  $n \in \mathbb{Z}$  and thus the minibands are repeating in the energy in period of  $2\pi \frac{v_F\hbar}{L}$ . Mathematically this ambiguity in  $n$  originates from the ambiguity of  $\epsilon_j(\mathbf{q})$  by  $2\pi$  appearing in the eigenvalues  $e^{i\epsilon_j(\mathbf{q})}$ ,  $j = 1, 2, \dots, 6$ . Physically this repetition can be traced back to the excitation energy of the microscopic one-dimensional modes with the same momentum  $\mathbf{q}$ , i.e., for a given  $\mathbf{q}$ , there are different one-dimensional modes with energy  $2\pi \frac{v_F\hbar}{L} n$ ,  $n \in \mathbb{Z}$ . Thus we expect that this repetition will fill up within the band width of the original parent 1d band. Indeed, this is the band structure that we find from the tight-binding problem, where the certain unit structure repeats in energy.

## 2. Spectrum of Network

Next we analyze the band structure out of this scattering description. As apparent from the Fig 2, the spectrum features (i) Dirac cones at  $K$  and  $K'$ , (ii) flat bands, and (iii) quadratic band touchings at  $\Gamma$ -point, which are the features of the tight-binding band structure.

Now the crucial question is if these features are stable against the symmetric deformation of the scattering matrices. We see that the parameters that we can tune are  $\{t_A = t_B = t, v_F, \chi\}$ , which determine the scattering amplitudes at the nodes and the phase accumulated by the modes while they travel along the links. We find that the overall band structures remain the same. In particular, the flat bands always survive. See Fig. 2.

## Appendix B: Flat Band Wavefunctions

Here we reproduce a few standard phenomenology of the flat bands in our model. These include the zeros of the wavefunction in space and the “frustration” in the hopping Hamiltonians, which is what actually happens in a Lieb lattice. In particular, the former guarantees the existence of a single flat band. In the main text, we go beyond the standard analysis and show the appearance of many stable flat bands.

### 1. Presence of Zeros at Tri-junctions

We first demonstrate that the wavefunction of the flat bands has zeros at the tri-junctions, i.e., nodes of the honeycomb network. For this, we plot out  $|\psi_{\mathbf{q}}(\mathbf{R})|^2$  at the tri-junction site  $\mathbf{R}$  along a high-symmetry cut in the

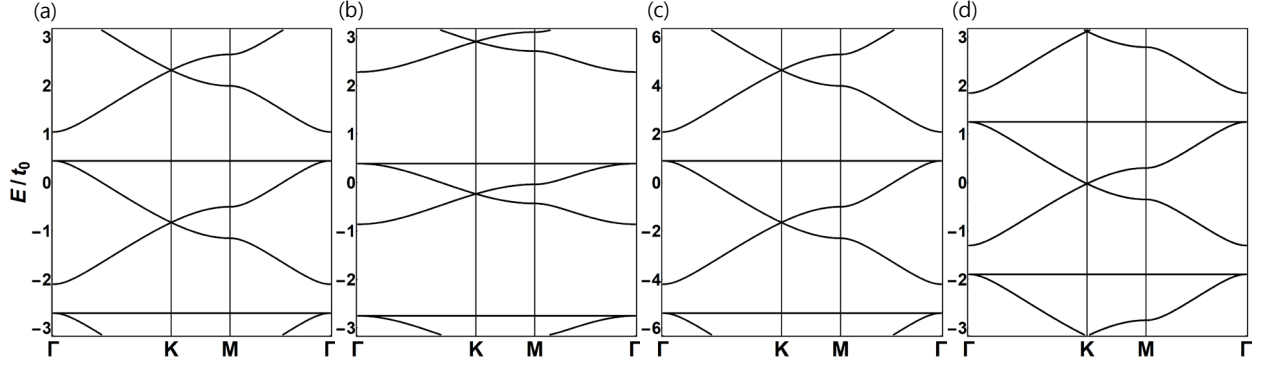


FIG. 2. Band structure of the network model for several different parameters. (a)  $t = 0.43$ ,  $v_F \hbar/L = 1$ ,  $\chi = 0.0$ , (b)  $t = 0.83$ ,  $v_F \hbar/L = 1$ ,  $\chi = 0.0$ , (c)  $t = 0.43$ ,  $v_F \hbar/L = 2$ ,  $\chi = 0.0$ , (d)  $t = 0.43$ ,  $v_F \hbar/L = 1$ ,  $\chi = 0.8$

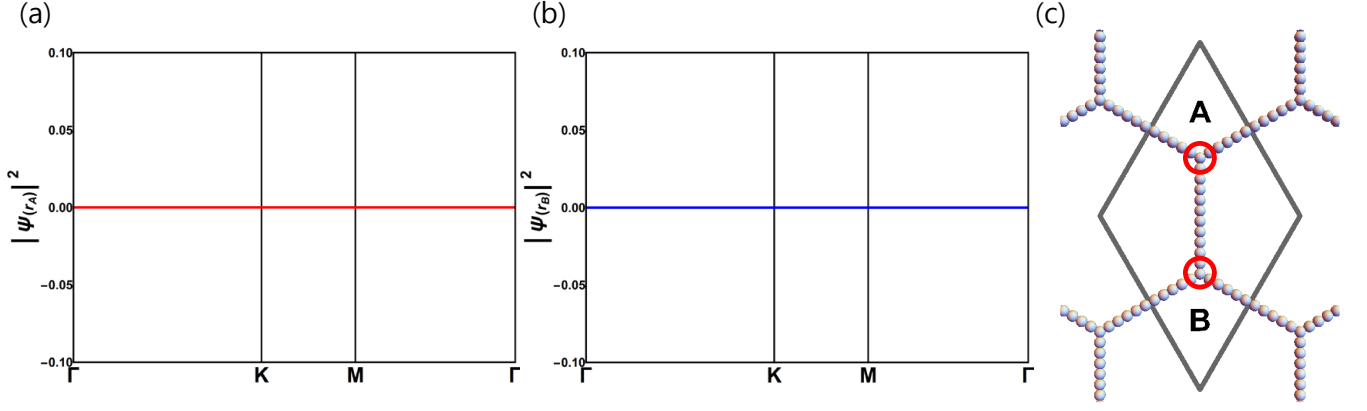


FIG. 3. The amplitude of Bloch wave function at junction sites in momentum space along the high-symmetry points. (a) is the amplitude at the junction A and (b) is the amplitude at the junction B. We are drawing here only along the high-symmetry cut, but one can confirm that the junction-site wavefunction vanishes everywhere in momentum space. (c) Network and the position of A and B junctions in the unit cell.

momentum space, where  $\psi_{\mathbf{q}}(\mathbf{r})$  is the Bloch function of the flat bands at the momentum  $\mathbf{q}$  and the site  $\mathbf{r}$  in a unit cell.

From Fig.3, we can clearly see that the Bloch function has zeros at the tri-junctions upto the numerical error. This confirms that the flat band states can be generated by the standing waves living in each wires. In fact, we can do better: from the Bloch state, we can even read off the sign structures of the non-dispersing states in the Fig 2 (A) of the main text. The Bloch states have a staggered  $\pm 1$  signs around the nodes, which is precisely the same structure as the wavefunction of the main text.

## 2. Proof of Existence of A Single Flat Band

For a few fine-tuned cases, we can in fact prove the existence of a single flat band. The case is that, there are odd number of sites between the tri-junctions and the Hamiltonian has only the nearest neighbor hoppings. For example, for the case with a single site inbetween the tri-junctions Fig. 4, we can factorize the Hamiltonian into the following:

$$H = - \begin{bmatrix} 0 & 0 & 0 & t_0 & t_0 e^{ika_2} \\ 0 & 0 & 0 & t_0 & t_0 e^{ika_1} \\ 0 & 0 & 0 & t_0 & t_0 \\ t_0 & t_0 & t_0 & 0 & 0 \\ t_0 e^{-ika_2} & t_0 e^{-ika_1} & t_0 & 0 & 0 \end{bmatrix} \quad (\text{B1})$$

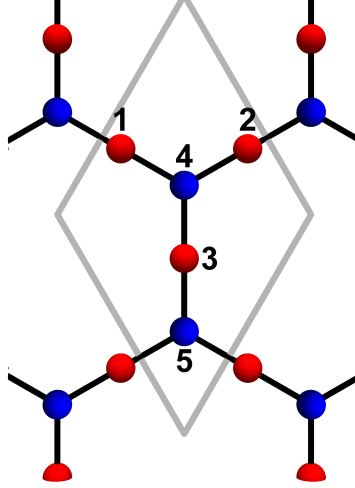


FIG. 4. Network with a single bridge site.

Since the Hamiltonian as a matrix has the rank less than its dimension, it must have an eigenvalue 0 for all the  $\mathbf{q}$ . This is the flat band because the corresponding eigenvalue is a constant zero over all the momentum  $\mathbf{q}$ . In fact, such factorization can be easily generalized into the cases with the odd number of sites between the tri-junctions. Suppose that  $(2m + 1)$ -sites exist between the tri-junctions, where  $m$  is an integer. Hence, there will be  $6m + 5$  sites per unit cell. We can let the adjacent lattice points be included in different sets A and B since the lattice is bipartite. Assuming that the lattice point at the junction is included in the set A without loss of generality, we find that the set A will have  $3m + 3$  sites and the set B will have  $3m + 2$  sites. Now, we index the lattice points in the set A with the integers from 1 to  $3m + 3$  and the lattice points in the set B with the integers from  $3m + 4$  to  $6m + 5$ . Then, since the matrix representation of the tight-binding Hamiltonian is zero for all  $(i, j)$  except when  $i$ -th and  $j$ -th lattice points are adjacent. This makes the Hamiltonian block-off-diagonal, where the blocks are  $(3m + 3) \times (3m + 3)$  and  $(3m + 2) \times (3m + 2)$  sized zero matrices. Hence, the rank of the matrix is lower than the dimension of the matrix by 1, which signals the emergence of the flat band. Fig.5 is an example. This honeycomb network has three sites between tri-junctions, and the sites are indexed following the above method. The Hamiltonian, which is  $11 \times 11$ , can be written as the two rectangular off-block-diagonal matrices.

However, we remark that such factorization is absent (at least we couldn't find it after some trials) for the generic cases with further neighbor hoppings. Hence, this approach cannot be used to prove the existence of many stable flat bands.

### Appendix C: Flat Bands with Rashba Spin-Orbit Coupling

Here we investigate the effect of the Rashba spin-orbit coupling on the flat bands. Here, the spin-orbit coupling is between the next nearest neighbor sites and we find that this coupling does not disperse the flat bands.

$$H = -t \sum_{\langle \mathbf{r}, \mathbf{r}' \rangle} (c_{\mathbf{r}}^{\dagger} c_{\mathbf{r}'} + h.c.) + i\lambda_R \sum_{\mathbf{r}, \mathbf{r}'} c_{\mathbf{r}}^{\dagger} \left[ (\vec{s} \times \hat{d}_{\mathbf{r}, \mathbf{r}'} ) \cdot \hat{z} \right] c_{\mathbf{r}'} + h.c., \quad (C1)$$

which has the spin-orbit coupling  $\lambda_R$  on top of the tight-binding model Eq.(1) of the main text. Here we set  $t_J = 0$ . We vary  $\lambda_R = x \cdot t$  with  $x \in [0, 1]$ . Over the range of  $x$ , we find the flat bands survive while the band touchings are splitted. See Fig.6.

Next, we include the domain electrons and also all the allowed Rashba spin-orbit couplings, i.e., between the sites within the domain walls, between the site in the domain and the site in networks, and between the sites within the network. This in general will include all the possible symmetry-allowed short-ranged hoppings and spin-orbit couplings. This does not disperse the flat bands much within the bulk gap. See Fig.7. This implies that in TaS<sub>2</sub>, even if we include the spin-orbit couplings of Ta atoms, the flat bands will remain intact.



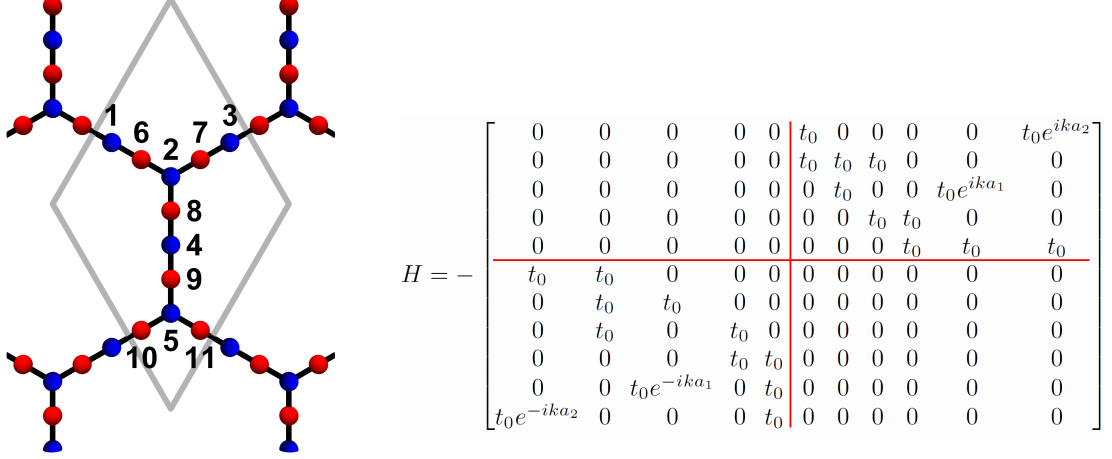


FIG. 5. (color online) A honeycomb with odd-sites between tri-junctions and only the nearest-neighbor hoppings. The blue sites were indexed from 1 to 5 and the red sites were indexed from 6 to 11. (right) A Hamiltonian matrix followed the indexing method. The red guide line indicates block matrices.

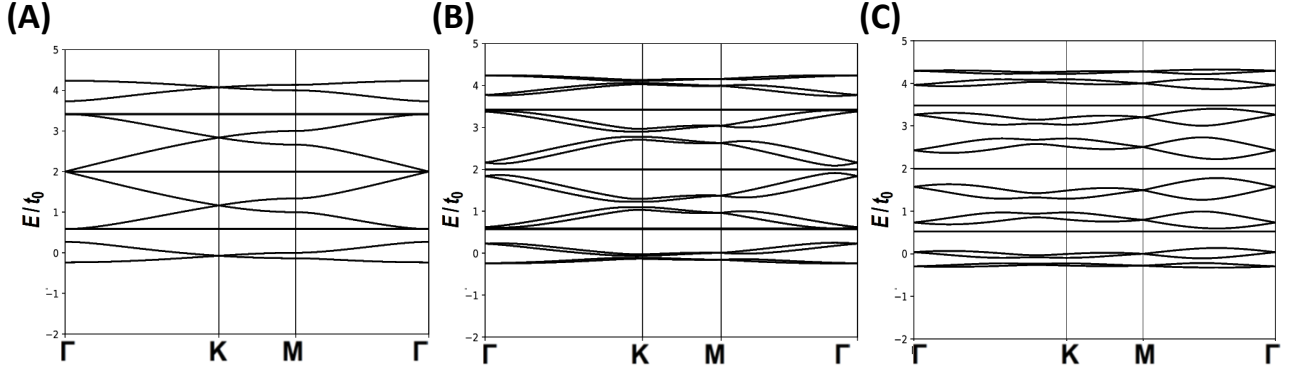


FIG. 6. (A) Band Structure of  $\lambda_R = 0$ . Note the spin-1 Dirac touching at  $\Gamma$  at  $E = 2t_0$ . (B) Band Structure of  $\lambda_R = 0.1t$  (C) Band Structure of  $\lambda_R = 0.3t$ . Note that the band touchings are lifted while the flat bands are intact.

#### Appendix D: No Stable Flat Bands for Triangular and Square Networks

We show that in the square or triangular network Fig. 8 and Fig. 9, we do not find any stable flat bands. This is consistent with the fact that there is no delicate destructive interference for these networks. Generically these two networks host the flat bands when there is only the nearest neighbor hoppings. However, they are removed as soon as the second neighbor hoppings are included.

#### Appendix E: Effect of Crystal Symmetry Breaking on Flat Bands

As illustrated in the main text, the very existence of the flat band heavily relies on the symmetry of the honeycomb network. This directly implies that the flat bands will be dispersive as soon as the protecting crystal symmetries are removed. In this supplemental information, we systematically break the crystal symmetries and show that indeed the flat bands are removed under the breaking of the symmetries. Note that the effect of the  $\mathcal{T}$ -symmetry breaking is in the main text, where we found the dispersive Chern bands.

The band structure of the lower-crystalline symmetries are shown in Fig.10. The matrix representation of the Hamiltonian follows the convention of Fig.5. The symmetries are broken by on-site potentials  $m$ . Note that the flat bands are removed in all the cases except  $C_3 \times R_x$  case where our argument in the main text straightforwardly

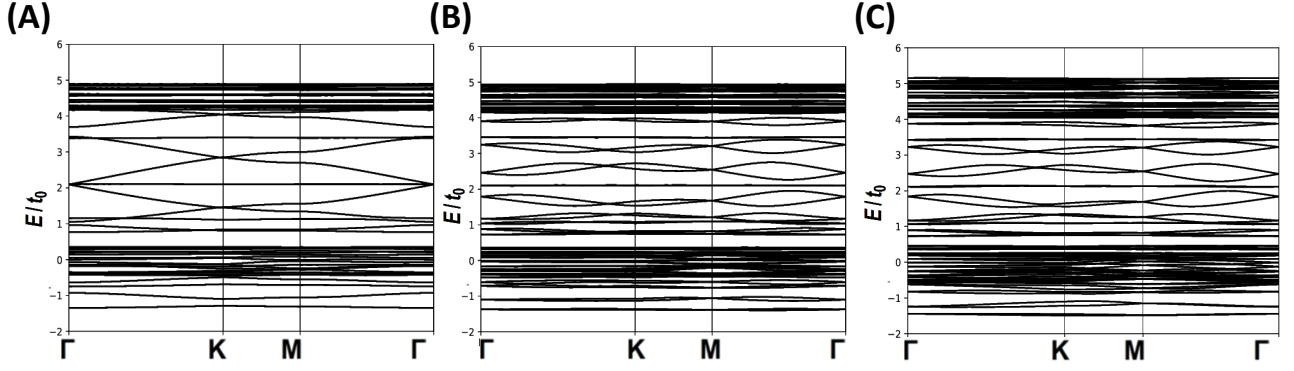


FIG. 7. (A) Band Structure of  $\lambda_R = 0$ . Note the spin-1 Dirac touching at  $\Gamma$  at  $E = 2t_0$ . (B) Band Structure of  $\lambda_R = 0.3t$  (for all the second neighbor hoppings) and non-zero spin-symmetric hopping parameters. (C) Band Structure of different  $\lambda_R$  for different pairs of the sites: i.e., two sites between the network, two sites between the domains, and between the domain and the network have the different spin-orbit couplings. Note that the band touchings are lifted while the flat bands are intact.

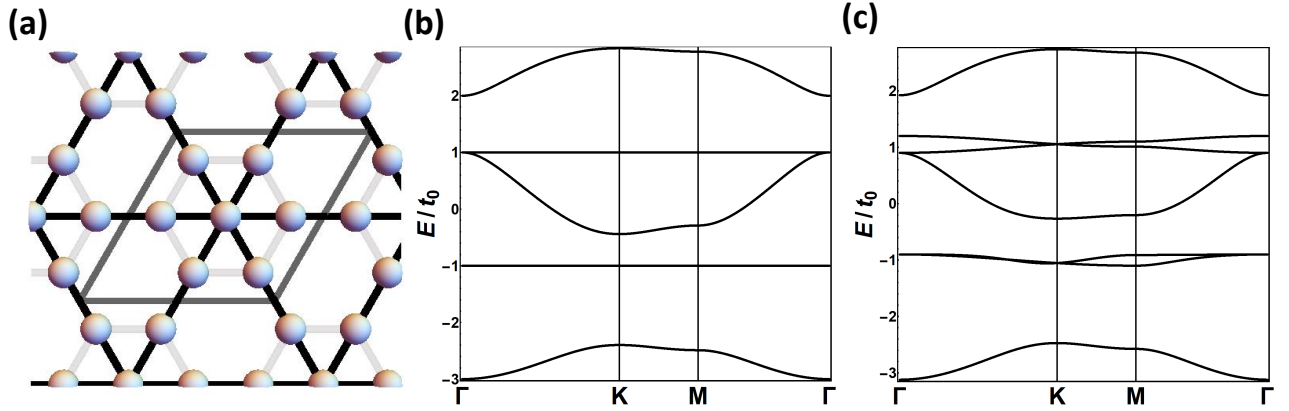


FIG. 8. (a) Triangular Network. (b) Spectrum with only the nearest neighbor hoppings. (c) Spectrum with weak second neighbor hoppings.

generalizes. From the previous work, we also have observed that  $C_3 \times R_x$  cannot lift the flat bands.<sup>1</sup>

## Appendix F: Details of BCS Calculations

Here we present the details of the BCS mean-field calculation. This involves the projection of the bare lattice-scale interactions to the BCS channels and the calculation of the mean-field gap equation and energy.

### 1. Coupling Constants

The microscopic pairing interaction that we introduced phenomenologically in the main text can be generally expressed as

$$H = U \sum_{\mathbf{R}, a} \hat{n}_{\mathbf{R};a}^2 + V \sum_{\mathbf{R}, \langle a, b \rangle} \hat{n}_{\mathbf{R};a} \hat{n}_{\mathbf{R};b} + V \sum_{\mathbf{R}, \mathbf{R}'} \hat{n}_{\mathbf{R};\text{end}} \hat{n}_{\mathbf{R}';\text{end}} \quad (\text{F1})$$

where  $U$  and  $V$  are real-valued constants,  $\hat{n}_{\mathbf{R};a}$  is the number operator at position  $\mathbf{R}$  and  $a$ -th site and  $a, b$  and “end” indicate the adjacent sites in real space. We are going to project this interaction terms to the BCS pairing term.

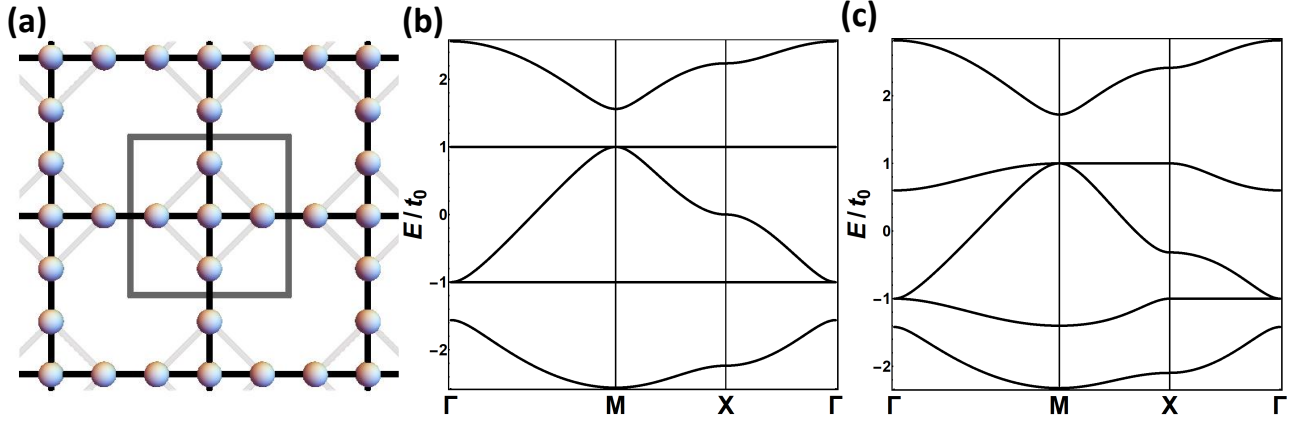


FIG. 9. (a) Square Network. (b) Spectrum with only the nearest neighbor hoppings. (c) Spectrum with weak second neighbor hoppings.

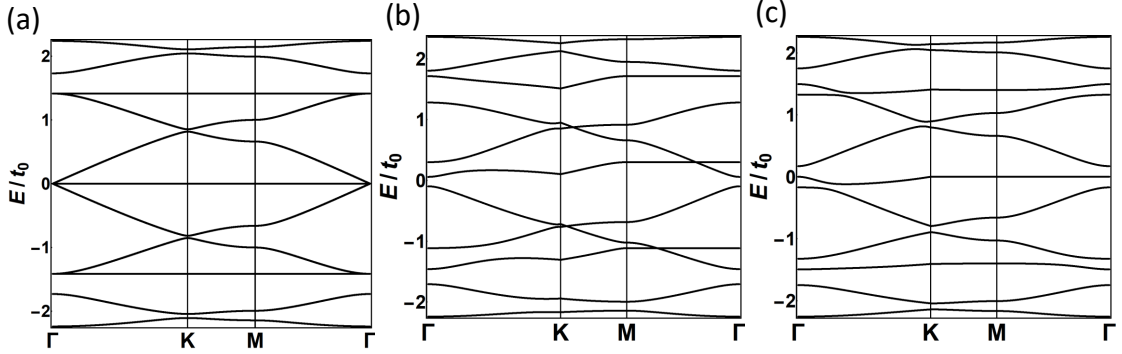


FIG. 10. Band Structure of symmetry-broken honeycomb network. The symmetries of the corresponding Hamiltonian are (a)  $C_3 \times R_x$  symmetry, (b)  $C_2$  and  $R_x$  symmetry, (c)  $C_2$  symmetry.

First, we consider the spin degree of freedom then the first term can be expanded.

$$U \sum_{\mathbf{R},a} \hat{n}_{\mathbf{R};a}^2 = U \sum_{\mathbf{R},a} (\hat{n}_{\mathbf{R};a\uparrow} + \hat{n}_{\mathbf{R};a\downarrow}) (\hat{n}_{\mathbf{R};a\downarrow} + \hat{n}_{\mathbf{R};a\uparrow}) \quad (\text{F2})$$

We only select  $n_{\uparrow}n_{\downarrow}$  pairs in this expansion since we are interested in the conventional BCS channel. By using the Fourier transformation, the first pairing term becomes

$$= \frac{2U}{N} \sum_{\mathbf{k}\mathbf{p}} \sum_{\mathbf{q}\mathbf{l}} \left[ \delta(\mathbf{q} + \mathbf{p} - \mathbf{l} - \mathbf{k}) F^U(\mathbf{p}, \mathbf{q}; \mathbf{l}, \mathbf{k}) \psi_{\mathbf{p}\uparrow}^{\dagger} \psi_{\mathbf{k}\uparrow} \psi_{\mathbf{q}\downarrow}^{\dagger} \psi_{\mathbf{l}\downarrow} \right] \quad (\text{F3})$$

where the form factor is defined as the following.

$$F^U(\mathbf{p}, \mathbf{q}; \mathbf{l}, \mathbf{k}) = \sum_a u_{\mathbf{k};a} u_{\mathbf{p};a}^* u_{\mathbf{q};a}^* u_{\mathbf{l};a} \quad (\text{F4})$$

Restricting the momentum summation into the pairing channels only, we obtain the BCS channel.

$$\begin{aligned} U \sum_{\mathbf{R},a} \hat{n}_{\mathbf{R};a}^2 &= 2U \sum_{\mathbf{k},\mathbf{p}} F_{BCS}^U(\mathbf{p}, \mathbf{k}) \psi_{\mathbf{p}\uparrow}^{\dagger} \psi_{-\mathbf{p}\downarrow}^{\dagger} \psi_{-\mathbf{k}\downarrow} \psi_{\mathbf{k}\uparrow} \\ F_{BCS}^U(\mathbf{p}, \mathbf{k}) &= \sum_a u_{\mathbf{k};a} u_{\mathbf{p};a}^* u_{-\mathbf{p};a}^* u_{-\mathbf{k};a} \end{aligned} \quad (\text{F5})$$

Similarly, we calculated the second and the third terms also.

$$V \sum_{\mathbf{R}, \langle a, b \rangle} \hat{n}_{\mathbf{R};a} \hat{n}_{\mathbf{R};b} + V \sum_{\mathbf{R}, \mathbf{R}'} \hat{n}_{\mathbf{R};\text{end}} \hat{n}_{\mathbf{R}';\text{end}'} = V \sum_{\mathbf{k}, \mathbf{p}} F_{BCS}^V(\mathbf{p}, \mathbf{k}) \psi_{\mathbf{p}\uparrow}^\dagger \psi_{-\mathbf{p}\downarrow}^\dagger \psi_{-\mathbf{k}\downarrow} \psi_{\mathbf{k}\uparrow} \quad (\text{F6})$$

$$F_{BCS}^V(\mathbf{p}, \mathbf{k}) = \sum_{\langle a, b \rangle} u_{\mathbf{p};a} u_{\mathbf{k};a}^* u_{-\mathbf{p};b}^* u_{-\mathbf{k};b}$$

Thus,

$$H = \sum_{\mathbf{k}, \mathbf{p}} (2U F_{BCS}^U + V F_{BCS}^V) \psi_{\mathbf{p}\uparrow}^\dagger \psi_{-\mathbf{p}\downarrow}^\dagger \psi_{-\mathbf{k}\downarrow} \psi_{\mathbf{k}\uparrow} \quad (\text{F7})$$

$$= \sum_{\mathbf{k}, \mathbf{p}} g(\mathbf{p}, \mathbf{k}) \psi_{\mathbf{p}\uparrow}^\dagger \psi_{-\mathbf{p}\downarrow}^\dagger \psi_{-\mathbf{k}\downarrow} \psi_{\mathbf{k}\uparrow}$$

Next, we further perform the expansion of  $g(\mathbf{p}, \mathbf{k})$  in terms of the angular momentum sectors, i.e., the s-wave and the d-wave channels.

$$g(\mathbf{p}, \mathbf{k}) = \sum_l g_l F_l(\mathbf{k}) F_l^*(\mathbf{p}) \quad (\text{F8})$$

## 2. Mean-Field Solution and Energy

We define the pairing order parameter.

$$\Delta_l = g_l \sum_{\mathbf{k}} F_l(\mathbf{k}) \langle \psi_{l;-\mathbf{k}\downarrow} \psi_{l;\mathbf{k}\uparrow} \rangle \quad (\text{F9})$$

The form factor  $F_l(\mathbf{k})$  and the  $g_l$  is defined as

$$F_0(\mathbf{k}) = 1 \quad (\text{F10})$$

$$g_0 = 2U f_U^s + V f_V^s$$

for the s-wave case, and

$$F_2(\mathbf{k}) = \cos \sqrt{3} k_x + e^{\frac{2}{3}\pi i} \cos \left( \frac{\sqrt{3}}{2} k_x + \frac{3}{2} k_y \right) + e^{-\frac{2}{3}\pi i} \cos \left( -\frac{\sqrt{3}}{2} k_x + \frac{3}{2} k_y \right) \quad (\text{F11})$$

$$g_2 = 2U f_U^d + V f_V^d$$

for the d-wave case. Here  $\{f_U^l, f_V^l, l = s, d\}$  are the constants depending on a particular choosen flat band. They are obtained from the projection of the BCS channel interactions into the particular pairing channels Eq.(F8). See the tables below.

	$f_U^s$	$f_V^s$	$f_U^d$	$f_V^d$
1st	0.1000	0.0958	0.0214	0.0217
2nd	0.1000	0.0709	0.0214	0.0153
3rd	0.1000	0.0709	0.0214	0.0153
4th	0.1000	0.0957	0.0214	0.0217

TABLE I. Table of  $\{f_U^l, f_V^l, l = s, d\}$  for the system with four sites between the junctions. Note that the band index means the “n-th” lowest band.

With all of these, we can now perform the mean-field theory of Eq. (3) of the main text. Note that  $g_l$  should be



	$f_U^s$	$f_V^s$	$f_U^d$	$f_V^d$
1st	0.0833	0.1019	0.0178	0.0226
2nd	0.0833	0.0833	0.0178	0.0178
3rd	0.1111	0.0000	0.0238	0.0000
4th	0.0833	0.0833	0.0178	0.0178
5th	0.0833	0.1018	0.0178	0.0226

TABLE II. Table of  $\{f_U^l, f_V^l, l = s, d\}$  for the system with foive sites between the junctions. Note that the band index means the “n-th” lowest band.

negative to be attractive.

$$\begin{aligned}
H' &= g_l \sum_{\mathbf{p}} \left( F^*(\mathbf{p}) \psi_{l;\mathbf{p}\uparrow}^\dagger \psi_{l;-\mathbf{p}\downarrow}^\dagger \right) \sum_{\mathbf{k}} \left( F(\mathbf{k}) \psi_{l;-\mathbf{k}\downarrow} \psi_{l;\mathbf{k}\uparrow} \right) \\
&= g_l \sum_{\mathbf{p}} \left( F^*(\mathbf{p}) \psi_{l;\mathbf{p}\uparrow}^\dagger \psi_{l;-\mathbf{p}\downarrow}^\dagger - F^*(\mathbf{p}) \langle \psi_{l;\mathbf{p}\uparrow}^\dagger \psi_{l;-\mathbf{p}\downarrow}^\dagger \rangle + F^*(\mathbf{p}) \langle \psi_{l;\mathbf{p}\uparrow}^\dagger \psi_{l;-\mathbf{p}\downarrow}^\dagger \rangle \right) \\
&\times \sum_{\mathbf{k}} \left( F(\mathbf{k}) \psi_{l;-\mathbf{k}\downarrow} \psi_{l;\mathbf{k}\uparrow} - F(\mathbf{k}) \langle \psi_{l;-\mathbf{k}\downarrow} \psi_{l;\mathbf{k}\uparrow} \rangle + F(\mathbf{k}) \langle \psi_{l;-\mathbf{k}\downarrow} \psi_{l;\mathbf{k}\uparrow} \rangle \right) \\
&= \sum_{\mathbf{k}} \left( \Delta_l F^*(\mathbf{k}) \psi_{l;\mathbf{k}\uparrow}^\dagger \psi_{l;-\mathbf{k}\downarrow}^\dagger + \Delta_l^* F(\mathbf{k}) \psi_{l;-\mathbf{k}\downarrow} \psi_{l;\mathbf{k}\uparrow} \right) - \frac{|\Delta_l|^2}{g_l}
\end{aligned} \tag{F12}$$

Then, the BCS Hamiltonian is given as the following, ignoring the constant term for a moment.

$$H = \sum_{\mathbf{k}} \Phi_{\mathbf{k}}^\dagger \begin{bmatrix} \xi_{\mathbf{k}} & \Delta_l F^*(\mathbf{k}) \\ \Delta_l^* F(\mathbf{k}) & -\xi_{\mathbf{k}} \end{bmatrix} \Phi_{\mathbf{k}} \tag{F13}$$

where  $\Phi_{\mathbf{k}}$  is the Nambu spinor  $(\psi_{\mathbf{k}\uparrow}, \psi_{-\mathbf{k}\downarrow}^\dagger)^T$ . Here  $\xi_{\mathbf{k}} = \epsilon_{\mathbf{k}} - \mu$ .

The  $2 \times 2$  matrix of the SU(2) group can be expressed with the Pauli matrices.

$$\begin{bmatrix} \xi_{\mathbf{k}} & \Delta_l F^*(\mathbf{k}) \\ \Delta_l^* F(\mathbf{k}) & -\xi_{\mathbf{k}} \end{bmatrix} = \mathbf{n} \cdot \boldsymbol{\sigma} = |\mathbf{n}| \begin{bmatrix} \cos \theta & e^{-i\phi} \sin \theta \\ e^{i\phi} \sin \theta & -\cos \theta \end{bmatrix} \tag{F14}$$

We find the unitary matrix  $Q$  which diagonalize the Hamiltonian.

$$Q^\dagger H Q = \begin{bmatrix} |\mathbf{n}| & 0 \\ 0 & -|\mathbf{n}| \end{bmatrix} \tag{F15}$$

$$Q = \begin{bmatrix} \cos \frac{\theta}{2} & -e^{-i\phi} \sin \frac{\theta}{2} \\ e^{i\phi} \sin \frac{\theta}{2} & \cos \frac{\theta}{2} \end{bmatrix} \tag{F16}$$

Then we define states, which are number-conserving, using the eigenvectors.

$$\chi_{\mathbf{k}} = \begin{bmatrix} \alpha_{\mathbf{k}\uparrow} \\ \alpha_{-\mathbf{k}\downarrow}^\dagger \end{bmatrix} = Q^\dagger \Phi_{\mathbf{k}} \tag{F17}$$

$$\begin{aligned}
\alpha_{\mathbf{k}\uparrow} &= \cos \frac{\theta}{2} \psi_{\mathbf{k}\uparrow} + e^{-i\phi} \sin \frac{\theta}{2} \psi_{-\mathbf{k}\downarrow}^\dagger \\
\alpha_{-\mathbf{k}\downarrow} &= -e^{-i\phi} \sin \frac{\theta}{2} \psi_{\mathbf{k}\uparrow}^\dagger + \cos \frac{\theta}{2} \psi_{-\mathbf{k}\downarrow}
\end{aligned} \tag{F18}$$

The normalized BCS ground state is given as the following.

$$\begin{aligned}
|\Omega_s\rangle &= \Pi_{\mathbf{k}} \alpha_{\mathbf{k}\uparrow} \alpha_{-\mathbf{k}\downarrow} |\Omega\rangle \\
&= \Pi_{\mathbf{k}} \left( \cos \frac{\theta}{2} \psi_{\mathbf{k}\uparrow} + e^{-i\phi} \sin \frac{\theta}{2} \psi_{-\mathbf{k}\downarrow}^\dagger \right) \left( e^{-i\phi} \sin \frac{\theta}{2} \psi_{\mathbf{k}\uparrow}^\dagger - \cos \frac{\theta}{2} \psi_{-\mathbf{k}\downarrow} \right) |\Omega\rangle \\
&\sim \Pi_{\mathbf{k}} \left( \cos \frac{\theta}{2} - e^{-i\phi} \sin \frac{\theta}{2} \psi_{\mathbf{k}\uparrow}^\dagger \psi_{-\mathbf{k}\downarrow}^\dagger \right) |\Omega\rangle
\end{aligned} \tag{F19}$$

By definition of the pairing order parameter, we calculate it with the BCS ground state.

$$\begin{aligned}
\Delta_l &= g_l \sum_{\mathbf{k}} F(\mathbf{k}) \langle \Omega_s | \psi_{-\mathbf{k}\downarrow} \psi_{\mathbf{k}\uparrow} | \Omega_s \rangle \\
&= g_l \sum_{\mathbf{k}} \Pi_{\mathbf{p},\mathbf{q}} F(\mathbf{k}) \langle \Omega | (\cos \frac{\theta}{2} - e^{i\phi} \sin \frac{\theta}{2} \psi_{-\mathbf{p}\downarrow} \psi_{\mathbf{p}\uparrow}) \psi_{-\mathbf{k}\downarrow} \psi_{\mathbf{k}\uparrow} (\cos \frac{\theta}{2} - e^{-i\phi} \sin \frac{\theta}{2} \psi_{\mathbf{q}\uparrow}^\dagger \psi_{-\mathbf{q}\downarrow}^\dagger) | \Omega \rangle \\
&= -g_l \sum_{\mathbf{k}} F(\mathbf{k}) \sin \frac{\theta}{2} \cos \frac{\theta}{2} e^{-i\phi} \\
&\simeq -g_l \int d^2 \mathbf{k} F(\mathbf{k}) \frac{1}{2} \sqrt{1 - \frac{\xi_{\mathbf{k}}^2}{\xi_{\mathbf{k}}^2 + |\Delta_l F^*(\mathbf{k})|^2}} \frac{\Delta_l F^*(\mathbf{k})}{|\Delta_l F^*(\mathbf{k})|}
\end{aligned} \tag{F20}$$

Assuming that the Fermi energy is exactly at the flat band, we have  $\xi_{\mathbf{k}} = 0$ .

$$\frac{1}{g_l} \simeq - \left( \frac{1}{2} \int d^2 \mathbf{k} |F(\mathbf{k})| \right) \frac{1}{|\Delta_l|} \tag{F21}$$

Finally, we can get the BCS mean-field energy.

$$\begin{aligned}
\Delta E &= E_{SC} - E_N \\
&= \left( - \int d^2 \mathbf{k} \sqrt{\xi_{\mathbf{k}}^2 + \Delta_l^2 |F(\mathbf{k})|^2} - \frac{|\Delta_0|^2}{g_l} \right) - \int d^2 \mathbf{k} \xi_{\mathbf{k}} \\
&= \frac{|\Delta_0|^2}{g_l} = \left( \frac{1}{2} \int d^2 \mathbf{k} |F(\mathbf{k})| \right)^2 g_l
\end{aligned} \tag{F22}$$

As the result of the numerical calculation, the BCS mean-field energies for each possible superconductor type are

$$\Delta E/A^2 \simeq \begin{cases} 0.25 \times (V f_V^s + 2U f_u^s) & (\text{s-wave SC}) \\ 0.2042 \times (V f_V^d + 2U f_u^d) & (\text{d-wave SC}) \end{cases} \tag{F23}$$

where  $A$  is area of the Brillouin zone. With the BCS mean-field energy, we draw the phase diagrams for the tight-binding honeycomb network models. Only the nearest-neighbor hoppings were considered. For the completeness, we also have included the ferromagnetism in Fig.11. The phase diagrams are drawn at each flat band of the model. We may turn on the next-nearest-neighbor hoppings, but the phase diagrams were slightly changed but they do not induce much difference.

Note that, when  $U$  is small, then the window for the  $d$ -wave SC is also small. However, when  $U$  is sizable and positive, then the window for the  $d$ -wave is also large.

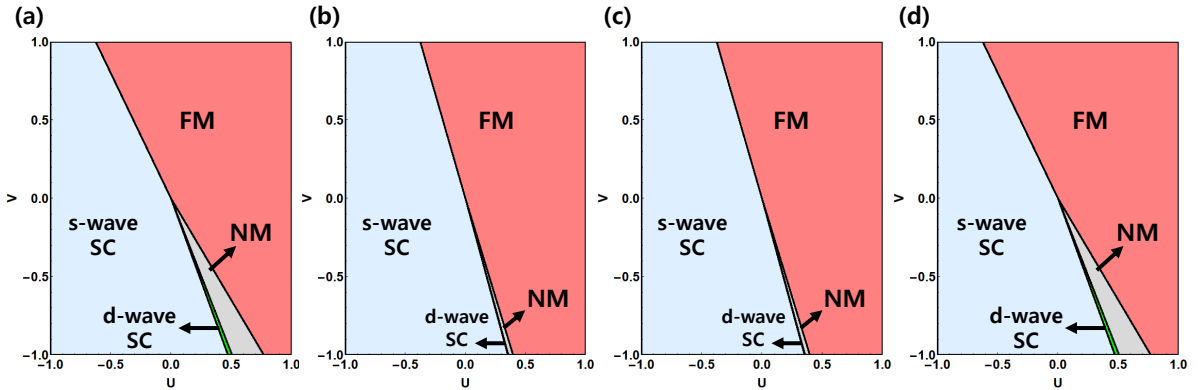


FIG. 11. Phase diagrams of flat bands of the tight-binding honeycomb network model with 4-bridge sites including the ferromagnetism. (a) the lowest-energy flat band, (b) the second-lowest-energy flat band, (c) the second-highest-energy flat band, (d) the highest-energy flat band. Note that there is always a window for the  $d$ -wave superconductors inbetween the  $s$ -wave superconductor and the normal metals for  $U > 0$ .

### 3. BdG Fermion Spectrum

We draw the BdG fermion spectrum.

$$\begin{aligned}\xi_{\mathbf{k}} &= \epsilon_0 \tau^0 + \sum_{i=1}^3 \epsilon_i \tau^i \\ &= \frac{1}{2m} \begin{bmatrix} (k_x + k_y)^2 & k_x^2 - k_y^2 \\ k_x^2 - k_y^2 & (k_x - k_y)^2 \end{bmatrix},\end{aligned}\tag{F24}$$

which has the flat band with the quadratic band touching at  $\mathbf{k} = 0$ . With the BCS pairing interaction, the fermion spectrum becomes the following.

$$E(\mathbf{k}) = \pm \sqrt{(k^2 \pm k^2)^2 / 4m^2 + |\Delta_l F(\mathbf{k})|^2},\tag{F25}$$

hence there are four bands at the low-energy limit. The BdG fermion spectra of the s-wave and the d-wave are plotted in Fig.12 near the  $\Gamma$ -point. Starting from the QBT with a flat band, the band gap are opened by the pairing interaction symmetrically. Note that they are gapped for the s-wave and gapless with doubled quadratic band touchings for the d-wave at the  $\Gamma$ -point. This state potentially has an interesting quantum critical behavior, which we leave for the future study.

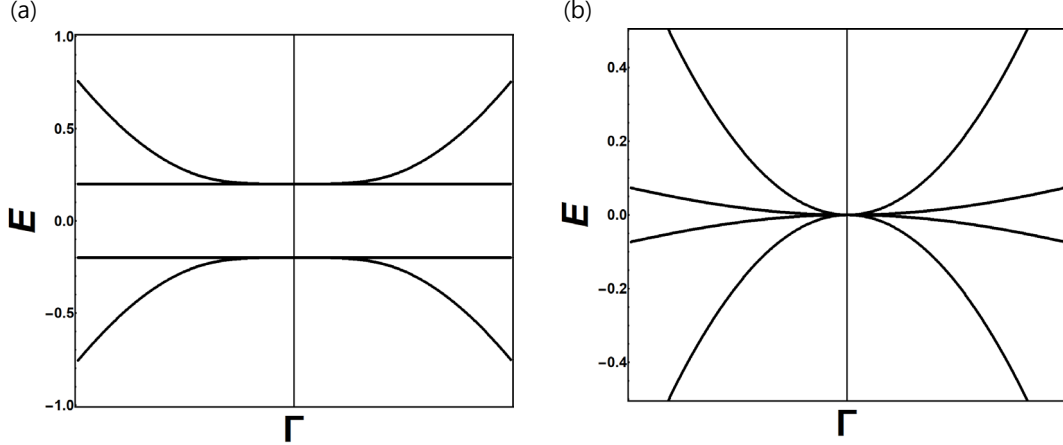


FIG. 12. The BdG spectrum for (a) the s-wave superconductor and (b) the d-wave superconductor near the  $\Gamma$ -point.

### Appendix G: Corner States at Tri-Junctions

In this supplemental information, we provide a few concrete realizations of the zero-dimensional states localized at the tri-junctions (or nodes) of the honeycomb network. We concentrate on the half-filled per wire case, in which the leading insulating instability is the period-2 charge-density waves.

The zero-dimensional states is the soliton of the charge-density waves, and they carry the fractional quantum numbers, e.g., the electric charge. Here we assume  $SU(2)$  symmetry and so consider effectively spinless fermions. Now, imagine that the tri-junction induces the frustrations for the charge-density wave order parameters between the neighboring links of the honeycomb plaquette. Due to the commensurability of the filling, the only allowed frustration is the  $\pi$ -phase shift between the neighboring links and is trapped at the junction. Once such mode is trapped at the junction, it cannot move around when the crystalline symmetries are protected. [Here we do not allow the Hilbert space to be changed when we consider the symmetric deformations of the model.] Then, we find that the 2d domains are insulating and its first-order boundaries are also insulating, but only its second-order boundary, i.e., the corner, has “in-gap” modes, which can be protected by the crystal symmetries. This is very parallel with the corner modes in the higher-order topology, (or more precisely, obstructed atomic insulator with the non-trivial nested Wilson loop topology).<sup>4-7</sup> Note that, in the reference<sup>8</sup>, the junctions of gapped wires are considered in an entirely different context, and the emergent corner states are discovered. Our finding is consistent with theirs.

It is well-known that, in 1d, a soliton of the period-2 charge density waves is the same as the boundary mode of the Su-Schrieffer-Heeger model. In fact, our construction here is essentially the charge-density wave versions of the higher-order topology. In this paper, we will not attempt to present the full theory and classification. Instead, we will present only the minimal contents, and the precise connection and classification of the “higher-order topological” domain wall states will be reported elsewhere.

### 1. Tight-Binding Models

Two examples of tight binding models exhibiting the localized corner state is shown in Fig.13. Because of the period-2 modulation, we modulate  $t$  and  $g$  in each link. Infinitesimal on-site energies,  $\pm m$ , were given at each junctions to break a symmetry weakly (this is commonly done in the investigation of the corner charge in higher-order topology and polarization chain).<sup>4-7</sup> They are explicitly written in Eq.G1 and Eq.G2. Then, we calculated the localized charges at each junction at half-filling. The charges at A(Red) and B(Blue) site showed opposite signs but their amplitude was nearly 0.5 when  $g$  is smaller enough than  $t$  (i.e., small correlation length limit). The better localization of electric charge is expected when more sites are assumed on the wires as the Su-Schrieffer-Higger model does.

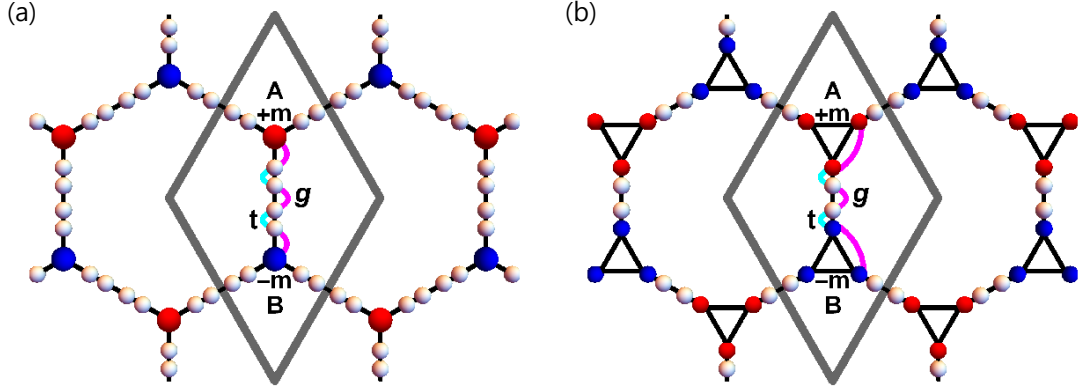


FIG. 13. (a) An unit cell(gray line) of the model is plotted in real space. Short and long atomic distances on the figure indicates hopping integrals  $t$  and  $g$  respectively. Infinitesimal on-site energy,  $+m$  and  $-m$ , were given at the site A and the site B. (b) The localized charge at each site, A(blue) and B(red), were plotted by the hopping integral's ratio. (c) A Hamiltonian matrix of the model in the momentum space.

$$H = - \begin{bmatrix} 0 & 0 & t & 0 & 0 & 0 & 0 & 0 & 0 & 0 & 0 & 0 & ge^{ika_2} \\ 0 & 0 & 0 & t & 0 & 0 & 0 & 0 & 0 & 0 & 0 & ge^{ika_1} & 0 \\ t & 0 & 0 & 0 & g & 0 & 0 & 0 & 0 & 0 & 0 & 0 & 0 \\ 0 & t & 0 & 0 & g & 0 & 0 & 0 & 0 & 0 & 0 & 0 & 0 \\ 0 & 0 & g & g & +m & g & 0 & 0 & 0 & 0 & 0 & 0 & 0 \\ 0 & 0 & 0 & 0 & g & 0 & t & 0 & 0 & 0 & 0 & 0 & 0 \\ 0 & 0 & 0 & 0 & 0 & t & 0 & g & 0 & 0 & 0 & 0 & 0 \\ 0 & 0 & 0 & 0 & 0 & 0 & g & 0 & t & 0 & 0 & 0 & 0 \\ 0 & 0 & 0 & 0 & 0 & 0 & 0 & t & 0 & g & 0 & 0 & 0 \\ 0 & 0 & 0 & 0 & 0 & 0 & 0 & 0 & g & -m & g & g & 0 \\ 0 & 0 & 0 & 0 & 0 & 0 & 0 & 0 & g & 0 & 0 & t & 0 \\ 0 & 0 & 0 & 0 & 0 & 0 & 0 & 0 & g & 0 & 0 & 0 & t \\ 0 & ge^{-ika_1} & 0 & 0 & 0 & 0 & 0 & 0 & 0 & t & 0 & 0 & 0 \\ ge^{-ika_2} & 0 & 0 & 0 & 0 & 0 & 0 & 0 & 0 & 0 & t & 0 & 0 \end{bmatrix} \quad (\text{G1})$$



$$H = - \begin{bmatrix} 0 & 0 & t & 0 & 0 & 0 & 0 & 0 & 0 & 0 & 0 & ge^{ika_2} \\ 0 & 0 & 0 & t & 0 & 0 & 0 & 0 & 0 & 0 & ge^{ika_1} & 0 \\ t & 0 & +m & g & g & 0 & 0 & 0 & 0 & 0 & 0 & 0 \\ 0 & t & g & +m & g & 0 & 0 & 0 & 0 & 0 & 0 & 0 \\ 0 & 0 & g & g & +m & t & 0 & 0 & 0 & 0 & 0 & 0 \\ 0 & 0 & 0 & 0 & t & 0 & g & 0 & 0 & 0 & 0 & 0 \\ 0 & 0 & 0 & 0 & 0 & g & 0 & t & 0 & 0 & 0 & 0 \\ 0 & 0 & 0 & 0 & 0 & 0 & t & -m & g & g & 0 & 0 \\ 0 & 0 & 0 & 0 & 0 & 0 & 0 & g & -m & g & t & 0 \\ 0 & 0 & 0 & 0 & 0 & 0 & 0 & g & g & -m & 0 & t \\ 0 & ge^{-ika_1} & 0 & 0 & 0 & 0 & 0 & 0 & t & 0 & 0 & 0 \\ ge^{-ika_2} & 0 & 0 & 0 & 0 & 0 & 0 & 0 & 0 & t & 0 & 0 \end{bmatrix} \quad (\text{G2})$$

These models are designed in the way that they trap the odd number of solitons at the tri-junction. Once the solitons are trapped, obviously they can be protected by the crystalline symmetries.

## Appendix H: Thermodynamics of Flat Bands

Here we compute the thermodynamic quantities of the flat bands. Since the contribution from the band touching will be negligible, we will take a completely flat band without the band touching here to compute the quantities.

### 1. Specific Heat

The total energy  $U$  is given as the following.

$$U = \int_0^\infty \epsilon D(\epsilon) f(\epsilon, T) d\epsilon \quad (\text{H1})$$

where  $f(\epsilon, T)$  is the Fermi-Dirac distribution. By the definition of the specific heat,

$$C = \frac{\partial U}{\partial T} = \int_0^\infty \epsilon D(\epsilon) \frac{\partial}{\partial T} \left( \frac{1}{e^{(\epsilon - \epsilon_F)/k_B T} + 1} \right) d\epsilon \quad (\text{H2})$$

The number of state at the flat band is  $N\delta(\epsilon - \epsilon_0)$  (with  $N$  being the number of states at the flat band) where  $\epsilon_0$  is the energy of the flat band.

$$C = \frac{N\epsilon_0(\epsilon_0 - \epsilon_F)}{k_B T^2} \frac{e^{(\epsilon_0 - \epsilon_F)/k_B T}}{(e^{(\epsilon_0 - \epsilon_F)/k_B T} + 1)^2} \quad (\text{H3})$$

Therefore, near the flat band,  $|\epsilon_0 - \epsilon_F| \ll k_B T$ , we find

$$C \sim \begin{cases} 0 & (\epsilon_0 = \epsilon_F) \\ \frac{1}{T^2} & (\epsilon_0 \neq \epsilon_F) \end{cases} \quad (\text{H4})$$

Note that, when the Fermi level is exactly at the flat band, the specific heat is always zero. We plot the specific heat in Fig.14. At the low-temperature limit, the specific heat is suppressed by  $\sim \exp(-|\epsilon_0 - \epsilon_F|/k_B T)$ .

### 2. Spin Susceptibility

We consider a spin-1/2 system where the both spin species have the same flat band energy at  $E_0$ . To compute the spin susceptibility, we apply the magnetic field  $h$  parallel to the z-axis.

$$H' = -h\sigma^z \quad (\text{H5})$$

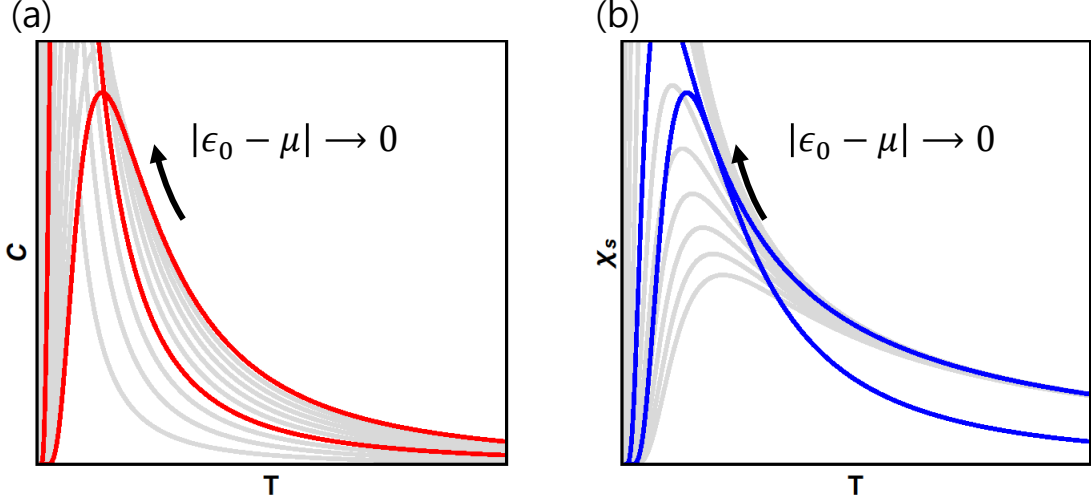


FIG. 14. Plot of the specific heat and the spin susceptibility of the flat bands.

The flat bands are split into two flat bands at  $(E_0 + h)$  for spin-down and  $(E_0 - h)$  for spin-up so the density of states is given as the following.

$$\begin{cases} D_{\uparrow}(\epsilon) = \frac{N}{2} \delta(\epsilon - (\epsilon_0 - h)) \\ D_{\downarrow}(\epsilon) = \frac{N}{2} \delta(\epsilon - (\epsilon_0 + h)) \end{cases}$$

The number of occupied electrons for each flat band is

$$N_{\sigma} = \int D_{\sigma}(\epsilon) f(\epsilon, \mu) d\epsilon \quad (\text{H6})$$

where  $\sigma = \uparrow, \downarrow$  and  $f(\epsilon, \mu)$  is the Fermi-Dirac distribution.

Magnetization is proportional to the difference of number of the spin-up and spin-down electrons.

$$\begin{aligned} m &= \frac{1}{2}(N_{\uparrow} - N_{\downarrow}) = \frac{N}{4} \int_0^{\infty} \left( \delta(\epsilon - (\epsilon_0 - h)) - \delta(\epsilon - (\epsilon_0 + h)) \right) \frac{1}{e^{(\epsilon - \mu)/k_B T} + 1} d\epsilon \\ &= \frac{N}{4} \left( \frac{1}{e^{(\epsilon_0 - h - \mu)/k_B T} + 1} - \frac{1}{e^{(\epsilon_0 + h - \mu)/k_B T} + 1} \right) \end{aligned} \quad (\text{H7})$$

By definition of the spin susceptibility,

$$\begin{aligned} \chi &= \left. \frac{\partial m}{\partial h} \right|_{h=0} \\ &= \frac{N}{2k_B T} \frac{e^{(\epsilon_0 - \mu)/k_B T}}{(e^{(\epsilon_0 - \mu)/k_B T} + 1)^2} \end{aligned} \quad (\text{H8})$$

The spin susceptibility near the flat band shows a similar tendency with the specific heat as indicated in Fig.14. The spin susceptibility is zero at the zero-temperature. As the fermi energy approach to the flat band energy, the spin susceptibility diverges at the zero-temperature.

---

\* Electronic Address: gilyoungcho@postech.ac.kr

<sup>1</sup> J. W. Park, G. Y. Cho, D. Cho, J. Lee, and H. W. Yeom, in preparation.

<sup>2</sup> J. Chalker and P. Coddington, Journal of Physics C: Solid State Physics **21**, 2665 (1988).

<sup>3</sup> D. K. Efimkin and A. H. MacDonald, Physical Review B **98**, 035404 (2018).

<sup>4</sup> W. A. Benalcazar, B. A. Bernevig, and T. L. Hughes, Science **357**, 61 (2017).

- <sup>5</sup> F. Schindler, A. M. Cook, M. G. Vergniory, Z. Wang, S. S. P. Parkin, B. A. Bernevig, and T. Neupert, *Science Advances* **4** (2018), 10.1126/sciadv.aat0346.
- <sup>6</sup> F. Schindler, Z. Wang, M. G. Vergniory, A. M. Cook, A. Murani, S. Sengupta, A. Y. Kasumov, R. Deblock, S. Jeon, I. Drozdov, H. Bouchiat, S. Guron, A. Yazdani, B. A. Bernevig, and T. Neupert, *Nature Physics* **14**, 918 (2018).
- <sup>7</sup> B. Kang, K. Shiozaki, and G. Y. Cho, arXiv preprint arXiv:1812.06999 (2018).
- <sup>8</sup> Y.-Q. Wang and J. E. Moore, *Phys. Rev. B* **99**, 155102 (2019).